

Particle Image Velocimetry Applications of Fluorescent Dye-Doped Particles

Brian Joseph Petrosky

Thesis submitted to the faculty of the Virginia Polytechnic Institute and State University in
partial fulfillment of the requirements for the degree of

Master of Science
In
Aerospace Engineering

Kevin T. Lowe
Wing F. Ng
William J. Devenport

May 6, 2015
Blacksburg, Virginia, USA

Keywords: Particle Image Velocimetry, Laser Induced Fluorescence, Kiton Red, Laser Flare

Copyright ©2015, Brian Joseph Petrosky

Particle Image Velocimetry Applications of Fluorescent Dye-Doped Particles

Brian Joseph Petrosky

Abstract

Laser flare can often be a major issue in particle image velocimetry (PIV) involving solid boundaries in a flow or a gas-liquid interface. The use of fluorescent light from dye-doped particles has been demonstrated in water applications, but reproducing the technique in an airflow is more difficult due to particle size constraints and safety concerns.

The following thesis is formatted in a hybrid manuscript style, including a full paper presenting the applications of fluorescent Kiton Red 620 (KR620)-doped polystyrene latex microspheres in PIV. These particles used are small and monodisperse, with a mean diameter of $0.87 \mu\text{m}$. The KR620 dye exhibits much lower toxicity than other common fluorescent dyes, and would be safe to use in large flow facilities.

The first sections present a general introduction followed by a validation experiment using a standard PIV setup in a free jet. This work was the first to demonstrate PIV using fluorescent KR620-doped microspheres in an airflow, and results from the experiment were compared to similar data taken using standard PIV techniques. For the free jet results, Mie-scattered and fluorescent PIV were compared and showed average velocities within 3% of each other at the nozzle exit. Based on the PIV validation requirements used, this was deemed to be more of an indication of nozzle unsteadiness rather than an error or bias in the data. Furthermore, fluorescent PIV data obtained vector validation rates over 98%, well above the standard threshold of 95%.

The journal article expands on the introductory work and analyzes testing scenarios where fluorescent PIV allows for velocity measurements much closer to a solid surface than standard, Mie-scattered PIV. The fluorescent signal from the particles is measured on average to be 320 ± 10 times weaker than the Mie scattering signal from the particles. This fluorescence-to-Mie ratio was found to be nonuniform, with the typical signal ratio for a single particle expected to fall between 120 and 870. This reduction in signal is counterbalanced by greatly enhanced contrast via optical rejection of the incident laser wavelength. Fluorescent PIV with these particles is shown to eliminate laser flare near surfaces, in one case leading to 63 times fewer spurious velocity vectors than an optimized Mie scattering implementation in a region more than 5 mm from an angled surface.

In the appendix, a brief summary of an experiment to characterize the temperature sensitivity of the KR620 dye is included. This experiment concluded that the KR620 particles did not exhibit sufficient temperature sensitivity to warrant further investigation at the time.

Acknowledgments

The completion of my master's degree has by no means been an individual effort. There are a number of people, some of which I'll thank individually below, who were essential to the completion of my research and degree.

First and foremost is my advisor, Dr. Todd Lowe. He first offered me the opportunity to work on this project in the spring of 2014 while I was still an undergraduate. A year ago, we could never have imagined where the project would currently be. This is a testament to his day-to-day leadership and feedback, which has been huge in keeping me motivated and headed in the right direction.

Second, I'd like to thank those at NASA Langley for their hard work into the project. No accomplishments would have been possible without their funding through the NASA ARMD Seedling Fund and NIA Cooperative Agreement NNL09AA00A. But beyond that, the contributions from Paul Danehy, Christopher Wohl, and Pacita Tiemsin into the development of the PIV seed particles provided a solid foundation into the work I carried out. I was simply able to springboard off of their successes.

Finally, I'd like to thank both the Aerospace and Ocean Engineering Department at Virginia Tech and the CREATE center. This school is truly home to me and provided me the opportunity to accomplish everything I have wanted and more. Special thanks are due to Dan Cadel and Tobias Ecker, who taught me how to think critically as a researcher and conduct quality experiments. I'd also like to thank Henry Murray, David Wisda, Tyler Englerth, Pietro Maisto, and everyone else that is a part of the CREATE center. The collaborative, open-door environment created here has made it easy for me to bounce ideas off of people or look for help on whatever issue I'm facing. Their support helped rapidly improve my progress in the project, and for that I am extremely grateful.

It's been a long and crazy journey through my undergraduate and graduate degrees at Virginia Tech, but I'm very proud of my work and honored at our group's accomplishments. While I'm excited to move onto the next phase of my career, I can't wait to see how the impacts of this research grow over the years.

Table of Contents

Abstract.....	ii
Acknowledgments.....	iii
1. Introduction.....	1
1.1 Literature Review.....	1
1.2 Thesis Structure and Note on Contributors.....	4
1.3 Accomplishments Summary and Future Work.....	4
1.4. References.....	5
2. PIV Fundamentals and Benchtop Validation.....	7
2.1 Overview of PIV.....	7
2.2 Experimental Setup.....	9
2.2.1 Benchtop Validation Tests.....	9
2.2.2 Fluorescent PIV Application Tests.....	11
2.3 Fluorescent Particle Characterization.....	13
2.4 PIV Processing Vector Validation.....	13
2.5 Preliminary Test Results.....	14
2.6 References.....	17
3. Laser Flare Removal in Particle Image Velocimetry Using Fluorescent Dye-doped Particles.....	19
3.1 Abstract.....	19
3.2 Introduction.....	19
3.3 Methods.....	21
3.3.1 Kiton Red Polystyrene Latex Particles.....	21
3.3.2 Instrumentation and Experimental Setup.....	22
3.3.3 PIV Processing Vector Validation.....	23
3.4 Results.....	24
3.4.1 Fluorescence and Mie Signal Characterization.....	24
3.4.2 Near-surface PIV.....	27
3.5 Conclusions.....	33
3.6 Acknowledgements.....	33
3.7 References.....	34
4. Final PIV Conclusions.....	37
A. Appendix A: Kiton Red Thermometry.....	39
A.1 Introduction.....	39
A.2 Calibration Experiment Setup.....	40
A.3 Selection of Wavelength Bands.....	41
A.4 Temperature Measurement Uncertainty.....	42

A.5	Calibration Experimental Results	43
A.6	Conclusions	44
A.7	References	44

List of Figures

Figure 1.1. Illustration of laser flare from reflections off of a flat plate in an airflow.	1
Figure 1.2. The Stokes shift.	2
Figure 2.1. Standard 2D-PIV Test Configuration.	8
Figure 2.2. Simplified one-dimension discretized correlation plot.	9
Figure 2.3. Experimental PIV test setup for benchtop validation.	10
Figure 2.4. Fluorescent PIV application test setup.	11
Figure 2.5. (a) Parallel flat plate orientation, (b) rotated plate orientation and (c) plate dimensions. Flow is out of the page.	12
Figure 2.6. Measured emission spectrum of Kiton Red 620 doped PSLs collected from excitation with a continuous-wave laser at 532 nm. A spectral filter blocked the laser light.	13
Figure 2.7. Camera images of Mie scattered light (a) and KR620 fluorescent light (b). Images were taken at a nozzle exit velocity of 3.5 m/s. The images were not taken simultaneously.	15
Figure 2.8. Original camera image of Mie scattered light (a), single image processed PIV data of U- and V- velocities (b and c), and 15 image average U- velocity (d).	16
Figure 2.9. Original camera image of KR620 fluorescence (a), single image processed PIV data of U- and V- velocities (b and c), and 15 image average U- velocity (d).	16
Figure 2.10. Stream-wise velocity averages across nozzle exit.	17
Figure 3.1. Measured emission spectrum of Kiton Red 620 doped PSLs collected from excitation with a continuous-wave laser at 532 nm. A spectral filter blocked the laser light.	21
Figure 3.2. Experimental PIV test setup.	22
Figure 3.3. (a) Parallel flat plate orientation, (b) rotated plate orientation and (c) plate dimensions. Flow is out of the page.	23
Figure 3.4. Fluorescence-to-Mie average image correlation map, indicating spatial mapping between cameras.	24
Figure 3.5. 50 x 50 pixel image of fluorescence image (above) and Mie-scattered image (below).	25
Figure 3.6. Mie to fluorescence particle signal ratios.	26
Figure 3.7. Mie to fluorescence particle signal ratios. The center point represents the geometric mean of the data set and error bars are one geometric standard deviation above and below the mean.	26
Figure 3.8. Flat plate camera images for Fluorescent (left), Mie f/2.8 (middle), and Mie f/22 (right).	27
Figure 3.9. Background signal from laser flare.	28

Figure 3.10. Flat plate processing results at top for (a) Fluorescent (left), (b) Mie f/2.8 (center), and (c) Mie f/22 (right). Contour plots cover the area within 5 mm from the plate surface. Corresponding boundary layer velocity profiles for (d) Fluorescent, (e) Mie f/2.8, and (f) Mie f/22.	29
Figure 3.11. Falkner-Skan boundary layer profile comparison at (a) 40% chord (left), (b) 50% chord (middle), and (c) 60% chord (right).....	29
Figure 3.12. PIV images of (a) fluorescent particles (left) and (b) Mie particles (right).....	30
Figure 3.13. PIV images of (a) fluorescent particles (left) and (b) Mie particles (right) after background subtraction.....	30
Figure 3.14. Background signal from laser flare for angled flat plate.....	31
Figure 3.15. Angled flat plate processing results for (a) Fluorescent PIV f/2.8 (left), (b) Mie PIV f/32 (right).....	32
Figure A.1. Kiton Red thermometry test setup.	40
Figure A.2. Kiton Red particle fluorescent emission. Picture taken using optical filter to block all 532 nm laser light.	40
Figure A.3. Measured emission spectra of Kiton Red 620 doped PSLs at various temperatures.	41
Figure A.4. Kiton Red 620 PSL emission spectra normalized by the spectrum at 70°C.....	41
Figure A.5. Normalized two-band ratios for various wavelength bounds. Data sets were normalized by their measurements at 40°C.	42
Figure A.6. Nozzle exit temperature distribution across exit cross section.	43
Figure A.7. Kiton Red particle two-band filter ratio calibration curve. Best fit equation also shown.	43

List of Tables

Table 1.1. Present work using fluorescent light for PIV in an airflow.	3
Table 2.1. Vector validation rate comparison for benchtop fluorescent PIV.....	17
Table 3.1. Vector validation rate comparison.	32

1. Introduction

In the following section, a detailed look into work relevant to the author's is given, followed by a summary of the contents of the thesis and a look into the technology readiness of the experimental techniques presented by the current work.

1.1 Literature Review

Particle Image Velocimetry (PIV) is a widely used non-intrusive flow diagnostics tool. This imaging-based technique allows for accurate velocity measurements at any point in a flow illuminated by a laser sheet, and has had numerous applications in studying both laminar and turbulent flows [1]. PIV was first documented in the literature in 1984, most famously by Adrian [1, 2]. This technique was offered as a similar, but distinct, method for flow velocity measurement to Laser Speckle Velocimetry (LSV) [3]. The two differ in that PIV uses images of individual particles for calculating velocity rather than the speckle patterns formed from high particle source density in LSV. PIV quickly became the more popular of the two for fluid flows because LSV quickly loses accuracy in high velocity flows [4]. Further details of the basics of PIV can be found in Section 2.1.

In many PIV experiments, a solid boundary interacts with the flow, such as an airfoil or flow channel wall. When the laser light reaches the surface of these objects, light is reflected and creates glare on the images. This laser flare is detrimental because it decreases the signal to noise ratio (SNR) and possibly saturates the sensor pixels. In many instances, pixel blooming can also occur around saturations when photoelectrons leak into neighboring pixels, further expanding the imaging area affected by flare. In general, data in the presence of a glare are of low quality, if usable at all. Similar challenges also arise in liquid-gas flows, where light is reflected and refracted at the interface [5].

Figure 1.1 shows an example of the effects of laser flare on a camera image. In this test, PIV data is to be obtained of the airflow over a flat plate. The setup for this test is standard for PIV and is expanded upon in Section 2.2.2. When the laser is pulsed, reflections from the plate surface saturate the camera near the surface. In this region, it is impossible to track any particles and calculate a flow velocity. Furthermore, further away from the plate, secondary reflections off of other obstacles or boundaries in the test section create a significant background signal that make it difficult to distinguish seed particles. As will be

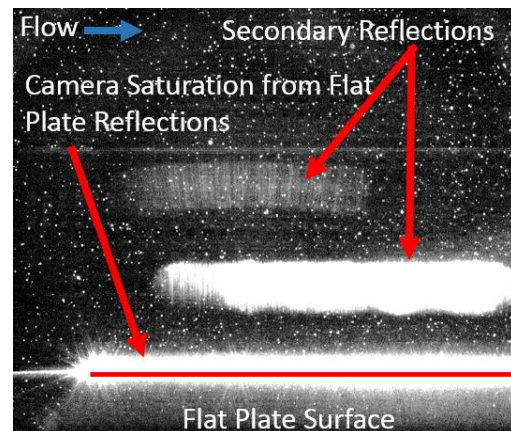


Figure 1.1. Illustration of laser flare from reflections off of a flat plate in an airflow.

shown in Section 3, this can seriously impact the accuracy of the resulting flow velocity calculations.

Many of the solutions for surface flare reduction involve modifications of the surface itself, including black paint [6], anodized black treatments [7], and clear models that match the index of refraction of the testing fluid [8]. Paterna et. al. [9] provide a good summary of the types of surface treatments that have been used for laser flare reduction, and concluded through tests of their own that the application of fluorescent paint onto the testing surface was the best method for reducing glare. This technique has been used in the past successfully by Konrath et. al. [10] using a Rhodamine B doped black paint. However, another application using a Rhodamine 6G fluorescent paint was unsuccessful in eliminating flare near the surface of the wing model being tested, where velocimetry data was unattainable within 5-10 mm of the surface [11].

The fluorescent paint technique is an example of laser induced fluorescence (LIF). The incident laser light, reflected light from surfaces, and Mie-scattered light from the seed particles

all occur at the same wavelength. When a fluorescent dye is excited by incident laser light, it emits light that is red-shifted relative to the incident light—the Stokes shift [12]. A brief overview of the physics involved is shown in Figure 1.2. A fluorescent molecule in its ground state will absorb a photon emitted from a laser source, taking it to a higher energy

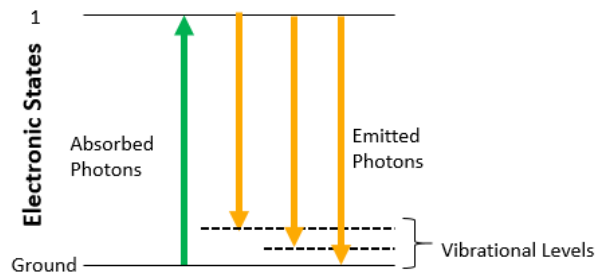


Figure 1.2. The Stokes shift.

state. Then, the molecule will emit a photon with less energy than the absorbed photon due to a combination of vibrational relaxation at the excited state and photon emission to the ground state at a higher vibrational level than the original state. Overall, the time involved in this process is on the order of nanoseconds [9]. With the Stokes shift, an appropriate optical filter can then be used to either pass only the fluorescent light or the Mie scattered light.

An alternative approach to the experiments presented above involves fluorescent particles. One may utilize the LIF signal from these particles for a variety of applications, including simultaneous temperature and velocity measurements [13, 14] or multi-stream flow tagging, for instance [15]. In the majority of applications in air, PIV data are taken using the Mie scattered light from the seed particles, while LIF is utilized by a second camera to obtain flow temperatures [16, 17]. Using fluorescent light for PIV, rather than Mie scattering, has been used on the macro scale in water flows [18, 19] and has had numerous applications in microscale PIV [20, 21]. The technique is more difficult to implement in a gas flow, which requires much smaller particles and safe dyes due to inhalation concerns [22, 23]. Research has shown that particle diameters near or below 1 μm are best for most airflows [24]. Fluorescent seed has been used on a few occasions for PIV in two phase flows, such as fuel injection into air [15, 25, 26]. These experiments

demonstrated the technique using seed particles as small as 1-5 μm [25], although the work by Towers et. al. reported difficulty imaging particles smaller than 4 μm [15]. Another past effort [27] in an air flow was successful and demonstrated the application of fluorescent particles for flare removal in PIV, but utilized potentially dangerous seed particles that required protective measures for use. A summary of previous work using fluorescent light for PIV in air is found in Table 1.1.

Table 1.1. Present work using fluorescent light for PIV in an airflow.

Primary Author	Seed Particle Size	Documented Mie/ Fluorescence Signal Difference?	Demonstrated Flare Removal?	Safe Particles?
Towers [15]	1-5 μm	Yes	No	No
Kosiwczuk [25]	1-5 μm	No	No	Yes
Driscoll [26]	Not Listed	No	No	No
Chennaoui [27]	< 1 μm	No	Yes	No
Rottenkolber [31]	< 3 μm	No	No	No
Lee [33]	> 6 μm	No	No	No
Angarita-James [34]	1.8 μm	No	No	No

The fluorescent light from seed particles can generally be expected to be a few orders of magnitude lower than the light from Mie scattering. The work by Towers et. al. [15] measured the fluorescence signal from 4-5 μm diameter Rhodamine 640 particles at 60 times weaker than the Mie scattered light from the same particles. The differences can be expected to become even more pronounced for small particles, because Mie scattered light scales with the square of the particle diameter (d_m^2) while fluorescent light scales with the cube of particle diameter (d_m^3), assuming a uniform fluorescent dye distribution over the particle volume [4].

Much of the past work with fluorescent dye-doped particles has involved the use of phosphor particles containing rare earth elements or other harmful chemicals such as toluene or Rhodamine [28, 29, 30, 31]. These chemicals can be dangerous and are unsafe to users in large flow facilities. Table 1.1 shows that no documented work to date has successfully demonstrated fluorescent PIV in an airflow using particles that meet the size and safety requirements for use in air. The present work has the focus of finding and applying safe fluorescent dyes to dope seed particles that can be used for LIF and flow diagnostics, especially PIV. Past work has centered around Dichlorofluorescein (DCF) and Kiton Red 620 (KR620) as safe alternatives for LIF, with KR620 exhibiting promising results [5, 23, 32]. The following discussions cover details of fluorescence yield for the KR620 safe particles and report a comparative study of Mie-scattering and fluorescent PIV for near-surface measurements.

1.2 Thesis Structure and Note on Contributors

The following thesis is formatted in a hybrid manuscript style and focuses on the advantages of using fluorescent particles for particle image velocimetry (PIV). Everything presented in the thesis was completely my own work, with one exception- researchers at NASA Langley were responsible for the production of the fluorescent seed particles used for testing. However, I designed, tested, analyzed, and documented all applications of these particles for fluorescent PIV in air.

The journal article included in the thesis, “Laser Flare Removal in Particle Image Velocimetry Using Fluorescent Dye-doped Particles,” has recently been submitted to the journal Measurement Science and Technology and is awaiting review. It is included in the thesis in its entirety. I conducted all experiments and analysis included in the paper using the same particles mentioned above. I wrote the paper and was given basic feedback from the co-authors.

Finally, in the appendix is a brief manuscript style summary of an experiment I conducted to characterize the temperature sensitivity of the KR620 dye.

1.3 Accomplishments Summary and Future Work

From the literature review in Section 1.1, it can be seen that laser flare is a significant and much researched problem in many PIV experiments involving flow over an object or an air-water interface. These near-surface regions of laser flare prevent the accurate calculation of flow velocity from PIV camera images. Furthermore, many common fluorescent dyes used in flow experiments are hazardous, and would be unsafe for use in a large flow facility.

The research included in this thesis uses the laser induced fluorescence (LIF) of polystyrene latex (PSL) microspheres doped with Kiton Red 620 dye to solve the issue of laser flare by blocking all surface reflected light with an optical filter and allowing only the fluorescent light from the seed particles to pass through to the camera. This work is the first known to the author to demonstrate flare removal in an airflow using fluorescent light from dye-doped seed particles that are both small enough for PIV in air and safe enough for use in open facilities. Sections 2 and 3 detail the experiments set up to validate the technique and demonstrate that fluorescent particles can be used to solve the problem with laser flare.

The work through the conclusion of this thesis would be considered to be about TRL Level 4. Further work is still necessary to demonstrate the work in larger facilities and higher speeds. There are no unique challenges to applying fluorescent PIV to high speed flows. The only obstacles in expanding this work to larger facilities are achieving a sufficient seed density and obtaining an adequate light signal from particles for PIV. While these are important considerations for any large PIV test, proper design of experiments for fluorescent PIV is key to

account for the weaker signal from fluorescent particles. Adjustments to laser sheet or camera optics may be necessary to optimize the fluorescent particle signal. However, the reduction in signal is counterbalanced by greatly enhanced near-surface particle tracking capabilities that allow for many measurements that would not otherwise be possible, which are described in later sections.

1.4. References

- [1] Adrian R J, "Twenty Years of Particle Image Velocimetry," *Experiments in Fluids*, vol. 39, no. 2, pp. 159-169, 2005.
- [2] Adrian R J, "Scattering Particle Characteristics and Their Effect on Pulsed Laser Measurements of Fluid Flow: Speckle Velocimetry vs. Particle Image Velocimetry," *Applied Optics*, vol. 23, no. 11, pp. 1690-1691, 1984.
- [3] Meynart R, "Equal Velocity Fringes in a Rayleigh-Benard Flow by a Speckle Method," *Applied Optics*, vol. 19, no. 9, pp. 1385-1386, 1980.
- [4] Adrian R and Westerweel J, *Particle Image Velocimetry*, New York: Cambridge University Press, 2011.
- [5] Petrosky B, Maisto P, Lowe K T, André M, Bardet P, Tiemsin P, Wohl C and Danehy P, "Particle Image Velocimetry Applications Using Fluorescent Dye-doped Particles," in *AIAA Scitech*, Kissimmee, 2015.
- [6] Wernet M P, "Development of Digital Particle Imaging Velocimetry for Use in Turbomachinery," *Experiments in Fluids*, vol. 28, no. 2, pp. 97-115, 2000.
- [7] Rostamy N, Sumner D, Bergstrom D J and Bugg J D, "Local Flow Field of a Surface-Mounted Finite Circular Cylinder," *Journal of Fluids and Structures*, vol. 34, pp. 105-122, 2012.
- [8] Uzol O, Chow Y C, Katz J and Meneveau C, "Unobstructed Particle Image Velocimetry Measurements within an Axial Turbo-pump Using Liquid and Blade with Matched Refractive Indices," *Experiments in Fluids*, vol. 33, no. 6, pp. 909-919, 2002.
- [9] Paterna E, Moonen P, Dorer V and Carmeliet J, "Mitigation of Surface Reflection in PIV Measurements," *Measurement Science and Technology*, vol. 24, no. 5, 2013.
- [10] Konrath R, Klein C, Schröder A and Kompenhans J, "Combined Application of Pressure Sensitive Paint and Particle Image Velocimetry to the Flow Above a Delta Wing," *Experiments in Fluids*, vol. 44, no. 3, pp. 357-366, 2007.
- [11] Watanabe S, Kato H, Kwak D, Shirotake M and Rinoie K, "Stereoscopic PIV Measurements of Leading Edge Separation Vortices on a Cranked Arrow Wing," *Measurement Science and Technology*, vol. 15, no. 6, 2004.
- [12] Lakowicz J R, *Principles of Fluorescence Spectroscopy*, New York: Springer Science & Business Media, 2007.
- [13] Peterson B, Baum E, Böhm B, Sick V and Dreizler A, "Evaluation of Toluene LIF Thermometry Detection Strategies Applied in an Internal Combustion Engine," *Applied Physics B*, vol. 117, no. 1, pp. 151-175, 2014.
- [14] Abram C, Fond B, Heyes A and Beyrau F, "High-speed Planar Thermometry and Velocimetry Using Thermographic Phosphor Particles," *Applied Physics B*, vol. 111, no. 2, pp. 115-160, 2013.
- [15] Towers D P, Towers C E, Buckberry C H and Reeves M, "A Colour PIV System Employing Fluorescent Particles for Two-Phase Flow Measurements," *Measurement Science and Technology*, vol. 10, no. 9, 1999.
- [16] Hishida K and Sakakibara J, "Combined Planar Laser-induced Fluorescence- Particle Image Velocimetry Technique for Velocity and Temperature Fields," *Experiments in Fluids*, vol. 29, no. 1, pp. S129-S140, 2000.
- [17] Carter C D, Donbar J M and Driscoll J F, "Simultaneous CH Planar Laser-induced Fluorescence and Particle Imaging Velocimetry in Turbulent Nonpremixed Flames," *Applied Physics B*, vol. 66, no. 1, pp. 129-132, 1998.
- [18] Poussou S and Plesniak M W, "Near-Field Flow Measurements of a Cavitating Jet Emanating From a Crown-Shaped Nozzle," *Journal of Fluids Engineering*, vol. 129, no. 5, 2006.

- [19] Lozano A, Barreras F, Fueyo N and Santodomingo S, "The Flow in an Oil/Water Plate Heat Exchanger for the Automotive Industry," *Applied Thermal Engineering*, vol. 28, no. 10, pp. 1109-1117, 2008.
- [20] Wereley S and Meinhard C D, "Recent Advances in Micro-Particle Image Velocimetry," *Annual Review of Fluid Mechanics*, vol. 42, pp. 557-576, 2010.
- [21] Singh A K, Cummings E B and Throckmorton D J, "Fluorescent Liposome Flow Markers for Microscale Particle-Image Velocimetry," *Analytical Chemistry*, vol. 73, no. 5, pp. 1057-1061, 2001.
- [22] Lowe K T, Maisto P, Byun G, Simpson R, Verkamp M, Danehy P, Tiemsin P and Wohl C, "Laser Velocimetry with Fluorescent Dye-Doped Polystyrene Microspheres," *Optics Letters*, vol. 38, no. 8, pp. 1197-1199, 2013.
- [23] Maisto P, Lowe K T, Byun G, Simpson R, Verkamp M, Danley J, Koh B, Tiemsin P, Danehy P and Wohl C, "Characterization of Fluorescent Polystyrene Microspheres for Advanced Flow Diagnostics," in *AIAA AMT Conference*, San Diego, 2013.
- [24] Melling A, "Tracer Particles and Seeding for Particle Image Velocimetry," *Measurement Science and Technology*, vol. 8, no. 12, 1997.
- [25] Kosiwczuk W, Cessou A, Trinité M and Lecordier B, "Simultaneous Velocity Field Measurements in Two-Phase Flows for Turbulent Mixing of Sprays by Means of Two-Phase PIV," *Experiments in Fluids*, vol. 39, no. 5, pp. 895-908, 2005.
- [26] Driscoll K D, Sick V and Gray C, "Simultaneous Air/Fuel-Phase PIV Measurements in a Dense Fuel Spray," *Experiments in Fluids*, vol. 35, no. 1, pp. 112-115, 2003.
- [27] Chennaoui M, Angarita-Jaimes D, Ormsby M P, Angarita-Jaimes N, McGhee E, Towers C E, Jones A C and Towers D P, "Optimization and Evaluation of Fluorescent Tracers for Flare Removal in Gas-Phase Particle Image Velocimetry," *Measurement Science and Technology*, vol. 19, no. 11, 2008.
- [28] Omrane A, Petersson P, Aldén M and Linne M A, "Simultaneous 2D Flow Velocity and Gas Temperature Measurements Using Thermographic Phosphors," *Applied Physics B*, vol. 92, no. 1, pp. 99-102, 2008.
- [29] Brübach J, Patt A and Dreizler A, "Spray Thermometry Using Thermographic Phosphors," *Applied Physics B*, vol. 83, no. 4, pp. 499-502, 2006.
- [30] Omrane A, Särner G and Aldén M, "2D-temperature Imaging of Single Droplets and Sprays Using Thermographic Phosphors," *Applied Physics B*, vol. 79, no. 4, pp. 431-434, 2004.
- [31] Rottenkolber G, Gindele J, Raposo J, Dullenkopf K, Hentschel W, Wittig S, Spicher U and Merzkirch W, "Spray Analysis of a Gasoline Direct Injector by Means of Two-Phase PIV," *Experiments in Fluids*, vol. 32, no. 6, pp. 710-721, 2002.
- [32] Danehy P, Tiemsin P, Wohl C, Verkamp M, Lowe T, Maisto P, Byun G and Simpson R, "Fluorescence-Doped Particles for Simultaneous Temperature and Velocity Imaging," *NASA Technical Memorandum*, pp. TM-2012-217768, 2012.
- [33] Lee J and Nishida K, "Simultaneous Flow Field Measurement of D.I. Gasoline Spray and Entrained Ambient Air by LIF-PIV Technique," *SAE Technical Paper Series*, pp. 2003-01-1115, 2003.
- [34] Angarita-Jaimes D, Towers C E and Towers D P, "Three-Component Multi-Phase Velocimetry Measurements on a GDI Spray Using Optically Efficient Fluorescent Tracers," *Experiments in Fluids*, vol. 52, no. 4, pp. 949-962, 2012.

2. PIV Fundamentals and Benchtop Validation

The following section provides a general overview of PIV, details the setup used for the experiments in this thesis, describes the fluorescent particles and data validation techniques used, and finally presents preliminary PIV results using the fluorescent particles. For a more detailed description of PIV, please see the textbook by Adrian and Westerweel [1]. Section 2.1 draws heavily on material from that text.

2.1 Overview of PIV

As stated in Section 1.1, PIV is a widely used flow diagnostics technique for measuring the instantaneous velocity field of a moving fluid. Typically, the measurements are of two (2D-PIV) or three (Stereographic PIV) components of velocity in a cross section of the flow, although volumetric PIV has also been used [1]. Because all tests included in this thesis used 2D-PIV, the focus of the following discussions only include this approach.

In PIV, a fluid flow is seeded with small particles that are assumed to follow the direction of flow around it. This assumption is valid if the slip velocity (the difference in velocity between the particles and moving fluid) is sufficiently low. A term closely related to a particle's slip velocity is the time constant, derived in [1] and given by Equation 2.1:

$$\tau_p = \frac{(\rho_p - \rho_f)d_p^2}{18\rho_f\nu_f\phi} \quad (2.1)$$

In Equation 2.1, ρ_p is the particle density, ρ_f is the fluid density, d_p is the particle diameter, ν_f is the fluid kinematic viscosity, and ϕ is a function related to the particle Reynolds number. Equation 2.1 shows that particles with low diameters and densities closely matching the surrounding fluid are desirable for low particle time constants, and therefore low slip velocities. For example, a 1.0 μm polystyrene latex particle in air will have a time constant of 3.9 μs . An acceleration of 100g would lead to a particle slip velocity of 3.9 mm/s. To limit the slip velocity, particles in an airflow are generally chosen to be near or below 1.0 μm in diameter [2].

A typical 2D-PIV test setup is pictured in Figure 2.1. A laser is pulsed twice in quick succession, with a cylindrical lens used to form the focused laser beam into a thin sheet. Generally, a dual-cavity or dual-head laser with overlapping beams is used [1]. The time between pulses varies based on the flow speed, but the rule of thumb is to choose a time between pulses where the particles in the image will move about 5 pixels [3]. Particles within the light sheet are illuminated by Mie scattered light off of the particles. A camera is positioned to take images of the illuminated particles, and their movements are tracked in order to calculate the resulting flow velocity. Before taking particle images, the camera must be calibrated. This calibration process is

done to map the camera image plane to the physical coordinates in the laser sheet plane that they are imaging.

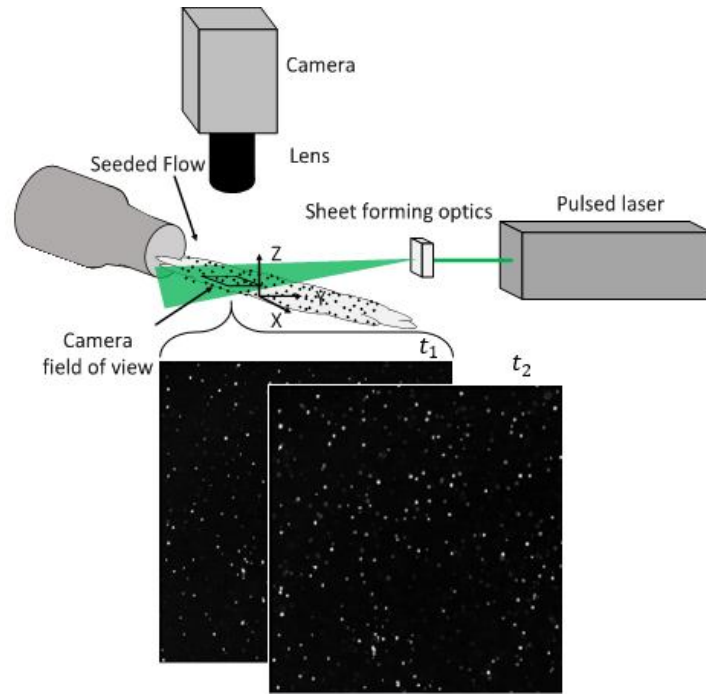


Figure 2.1. Standard 2D-PIV Test Configuration.

Individual particle motion is not tracked in PIV. Rather, successive images are broken up into small sections, known as interrogation windows, and the displacement of particles in an interrogation window W_1 from one image to the next is calculated using cross-correlation [1]:

$$R(s) = \int_{W_1} I_1(X) I_2(X + s) dX \quad (2.2)$$

In Equation 2.2, I_1 is the first image, I_2 is the second image, s is the displacement offset from one image to the next, and $R(s)$ is the resulting correlation value. The value of s for which $R(s)$ reaches a maximum is the correlation peak, which is chosen as the correct displacement of a group of particles in an interrogation window. High correlation values will occur when the particles in images 1 and 2 overlap closely for the displacement offset s . The flow velocity is calculated by dividing this displacement by the time in between pulses.

In reality, the cross correlation between images is discretized, as seen in Figure 2.2. While the figure is simplified in that it only shows displacements in one direction rather than two, it still illustrates the fluctuating values of the correlation function for given integer pixel displacements. In most digital PIV systems, the cross correlation is carried out using an FFT-based algorithm [3]. For subpixel accuracy, a smooth curve is interpolated over the discrete correlation peak, and the true peak calculated from the curve. This generally leads to a displacement precision on the order of 0.1-0.2 pixels [1].

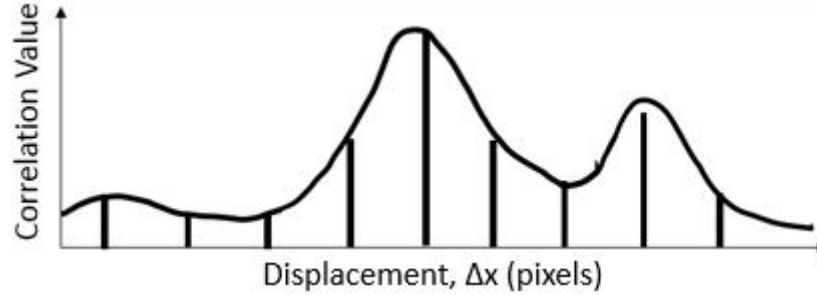


Figure 2.2. Simplified one-dimension discretized correlation plot.

A few “best practices” exist for optimal design of a PIV experiment that should be followed whenever possible [1]. They are all related but each represent a unique aspect of the experimental setup:

1. There should be at least 10 particle images in each interrogation window.
2. Less than 25% of the particles in an interrogation window should be lost in the second interrogation window due to in-plane particle motion. This is known as “in-plane loss of pairs.”
3. Less than 25% of the particles in an interrogation window should be lost in the second window due to out-of-plane motion of the particles.
4. The displacement variation from particles across an interrogation window should be less than the diameters of the particles in the image.

Failure to follow any of the above rules-of-thumb will result in a decrease in correlation and an increased probability of invalid peak detection (see Section 2.4).

2.2 Experimental Setup

The following sections detail the experimental setups used for the tests included in the thesis. Section 2.2.1 describes the test configuration for the initial fluorescent PIV validation tests. Then, in Section 2.2.2 is a thorough description of the test setup for the fluorescent PIV application tests.

2.2.1 Benchtop Validation Tests

A typical setup for 2D-PIV is seen in Figure 2.3. This set of experiments took place at Virginia Tech’s Vortical Flow and Diagnostics Lab (VTFD) and was used as a benchtop test to validate the use of KR620 doped particles for fluorescent PIV. The tests used a LaVision Imager Pro X 4M CCD camera with a 2048 x 2048 pixel resolution and processed the images using

LaVision's DaVis software [3]. The single camera (1) was positioned directly over the nozzle exit (2) and allowed for 2D velocimetry. The camera was mounted on a three piece aluminum frame attached to the optical table surface. A Sigma 105 mm f/2.8 EX DG macro lens (3) was used with the camera to obtain a close-up image of the flow. The camera lens was about 15 inches above the laser sheet plane, as shown in Figure 2.3. For fluorescence imaging, an Omega Optical 560 nm long pass filter (model 560HLP) was attached to the lens, blocking out all Mie scattered light from the particles and only allowing particle-emitted fluorescent light to be captured by the camera. A 532 nm double-pulsed Nd:YAG laser (4) was used at approximately 200 mJ/pulse to illuminate the flow and was controlled simultaneously with the camera by the DaVis software, recording at about 10 Hz. Finally, an $f = -25$ mm cylindrical lens (5) was used to form a thin laser sheet at the nozzle exit as indicated in Figure 2.3.

As stated in Section 1.1, KR620-doped PSL particles were used as seed for the testing. They were introduced into the flow using an Air-o-Swiss 7146 Ultrasonic Humidifier with a variable output setting to control how much seed was output. This vaporizer was placed in a mixing chamber, where it mixed with the air and flowed through a tube and finally a custom nozzle with an area ratio of 14.4:1 and exit diameter of $d = 14.15$ mm. The nozzle was mounted on a piece of 80/20 aluminum, which was then secured into place on the optical table to prevent the nozzle from moving during the test. The laser sheet extended approximately $3.15d$ from the nozzle exit, as illustrated in Figure 2.3. Finally, flow velocity was controlled using a Forney 75546 Air Line Mini-Regulator that attached to the compressed air hose used to run the nozzle.

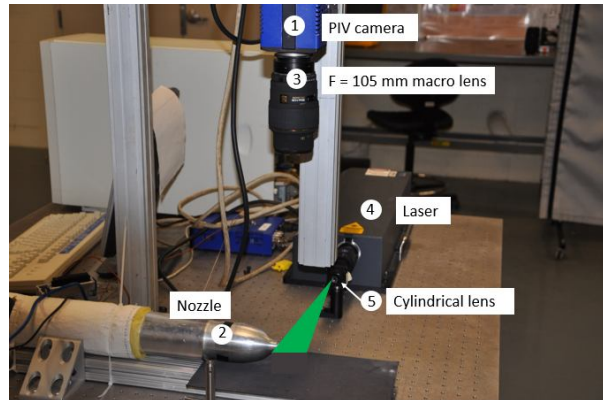


Figure 2.3. Experimental PIV test setup for benchtop validation.

Before each test, 50-75 mL of the KR620 particle solution were mixed with 50-75 mL of distilled water in equal proportions in an L&R Quantrex 90H ultrasonic disruptor to prevent particle agglomeration. Generally, much less than the amount prepared was used during a test day, but it was noticed that the vaporizer provided maximum seed output when it was near full. The mixture was removed from the disruptor and placed immediately into the vaporizer.

Tests were run at low speeds, on the order of 3.5 m/s, a speed that enabled optimal seeding densities for the vaporizer. During each test, 15 image sets were captured with the 560-nm filter on the lens with a lens f-stop of $f/2.8$. Immediately afterwards, the filter was removed and 15 additional Mie scattering images were taken with a lens f-stop of $f/22$. All tests were run at room temperature. Velocity vectors were obtained via cross-correlation of the two images in

each set, using a multi-pass technique in the DaVis software with 64 x 64 pixel initial and 32 x 32 pixel final interrogation windows and 50% overlap.

2.2.2 Fluorescent PIV Application Tests

The PIV data in Section 3 were recorded for the experimental setup seen in Figure 2.4 in the Newport News Shipbuilding-AOE Instructional Lab at Virginia Tech. Tests used either one or two Photron SA1.1 Fastcam high-speed cameras with a 1024 x 1024 pixel resolution and 12-bit intensity digitization. The cameras were positioned above and below the airflow and perpendicular to the laser sheet for 2D PIV. Camera 1 was mounted on a sliding rail, as seen in Figure 2.4b and Figure 2.4c, which was attached to a piece of 80/20 aluminum and secured to the optical table. Camera 2 was placed on a 3-axis traverse and 3-axis camera mount so that it could be maneuvered to image the same particles in the flow.

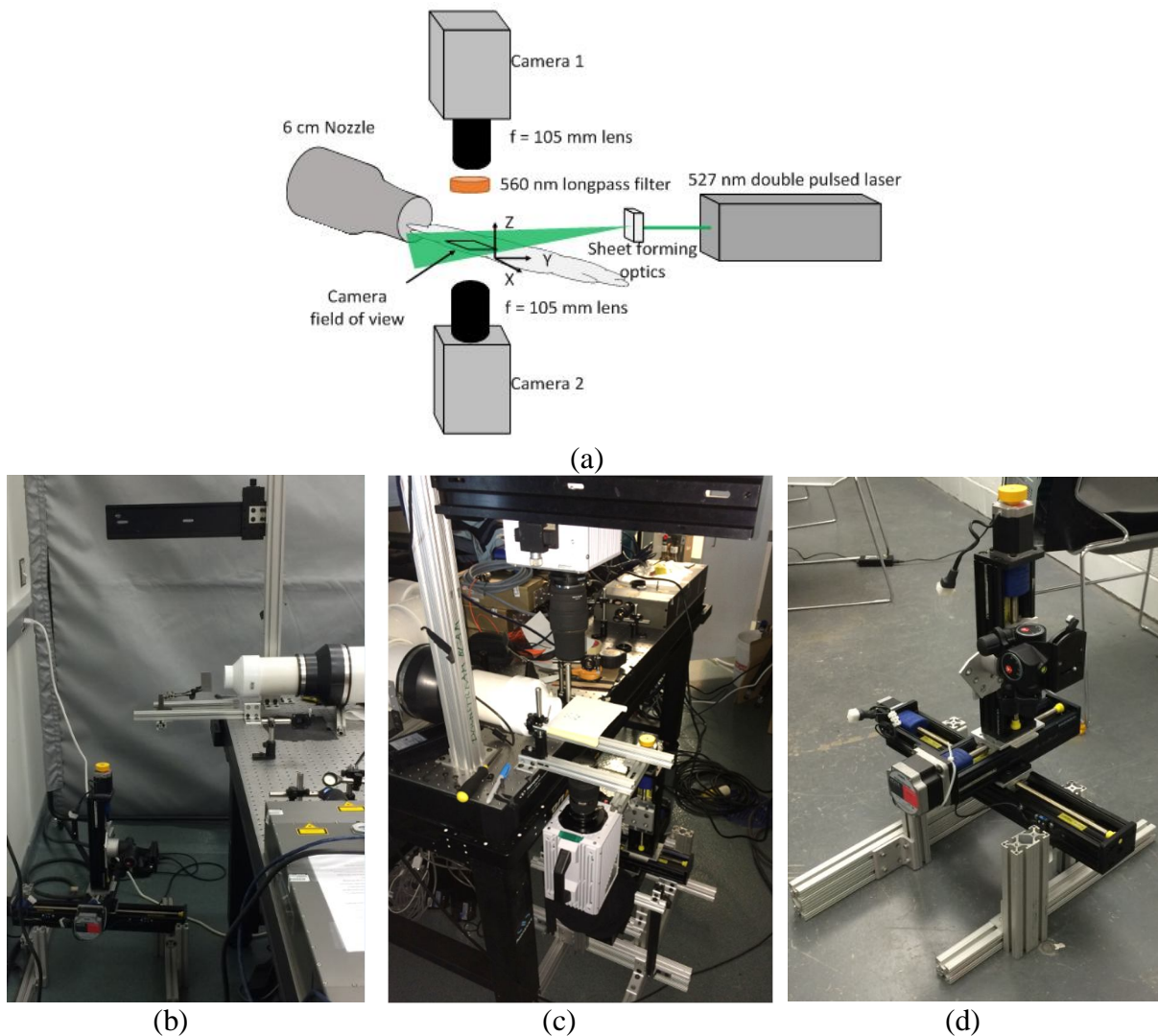


Figure 2.4. Fluorescent PIV application test setup.

The three Velmex traverses were configured as seen in Figure 2.4d to individually move Camera 2 in the x, y, or z direction using Cosmos 3.1.6 software. The distance from the lens edges to the laser sheet plane for both cameras was approximately 5 inches. The results of this testing are provided in Section 3.4.1. Two Sigma 105 mm f/2.8 EX DG macro lenses were used with the cameras to obtain a close-up image of the flow. The camera fields of view were $30.7 \times 30.7 \text{ mm}^2$ for single camera testing and $29.6 \times 29.6 \text{ mm}^2$ for the two camera testing.

For fluorescence imaging, an Omega Optical 560 nm long pass filter, model 560HLP, was attached to the lens, blocking out all Mie scattered light from the particles and only allowing particle-emitted fluorescent light to be captured by the camera. A 527 nm dual-head Nd:YLF laser (Photonics Model DM30) was used at approximately 23 mJ/pulse to illuminate the flow and was controlled simultaneously with the camera by LaVision's DaVis software [34], recording at 2.5 kHz for time-resolved images. The beam height had to be raised to coincide with the center of the nozzle exit. This was done using two high power mirrors, as seen on the right side of Figure 2.4b. Finally, an $f = -20 \text{ mm}$ cylindrical lens was used after the mirrors to form a thin laser sheet at the nozzle exit in the orientation depicted in Figure 2.4a. The laser sheet measured approximately 1.25 mm thick and 3.5 cm wide in the measurement plane at the nozzle exit. The cameras imaged a region of flow about 8 cm from the nozzle exit.

The KR620-doped PSL particles were seeded using two Air-o-Swiss 7146 ultrasonic humidifiers. Seed was introduced well upstream of the nozzle exit into the blower inlet, where it mixed with the air at room temperature and flowed through a nozzle of 6 cm exit diameter. The airflow at the exit for PIV tests was about 4.5 m/s, corresponding to a Reynolds number per meter of approximately $280,000 \text{ m}^{-1}$. Before each test, the KR620 particle solution was mixed in equal proportions with distilled water and sonicated for fifteen minutes in an L&R Quantrex 90H ultrasonic disruptor to prevent particle agglomeration. The mixture was then removed from the disruptor and placed immediately into the vaporizer.

Additional tests were run with a single camera; the setup remained the same as seen in Figure 2.4 except for the removal of Camera 2. In these tests, the near-surface flow over a blunt leading edge flat aluminum plate was measured. In the first test, seen in Figure 2.5a, the plate was oriented parallel to the flow exiting the nozzle and perpendicular to the incident laser sheet. In the second test, seen in Figure 2.5b, the

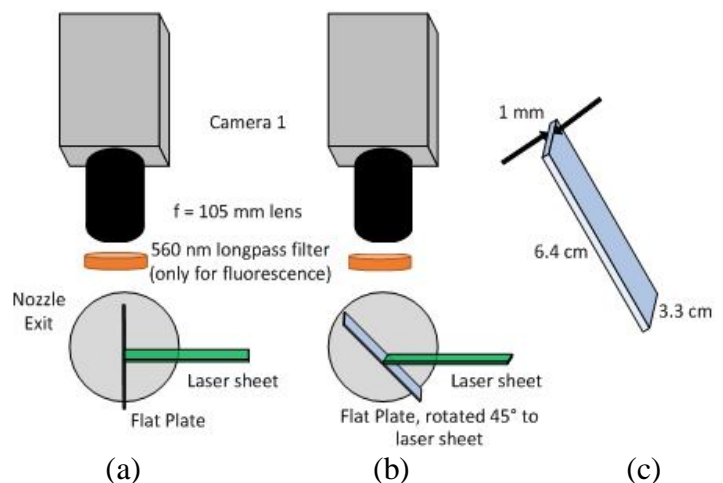


Figure 2.5. (a) Parallel flat plate orientation, (b) rotated plate orientation and (c) plate dimensions. Flow is out of the page.

plate was oriented 45° to the incident laser sheet but still parallel to the airflow. The dimensions of the flat plate are shown in Figure 2.5c. The plate was secured via a clamp placed on an 80/20 rail that extended out over the edge of the optical table, seen in Figure 2.4c. For these single-camera tests, a set of 2000 double-frame fluorescent images was obtained with the filter over the lens. Then, the filter was quickly removed and another 2000 double-frame images were recorded of the Mie-scattered light from the seed particles.

2.3 Fluorescent Particle Characterization

A common type of seed particle that has been used for PIV measurements is polystyrene latex (PSL) microspheres, due to their high index of refraction and low density [1]. Recent work at NASA Langley Research Center has refined the manufacturing techniques of these spherical microparticles to create a highly uniform and tunable size distribution on the order of $1 \mu\text{m}$ [4]. The KR620-doped PSL particles used in the present work had a $0.87 \mu\text{m}$ monodisperse diameter and were developed using an improved proprietary version compared to that initially described in [5], using a dispersion polymerization technique.

The fluorescence emission spectrum of the particles, after being atomized and dispersed in air, was measured by a Thorlabs CCS175 spectrometer (Figure 2.6). The peak fluorescence emissions occur within the wavelength range of 580 - 600 nm, such that a long pass filter with a cut-on wavelength between 532 nm and this range can be used to reject Mie scattering and only transmit fluorescent light.

The toxicity of KR620 is very low, making it a good candidate for use in large, open air applications. It falls in the lowest category of toxicity according to its Material Data Safety Sheet [6]. For comparison, two other common fluorescent dyes, Rhodamine B and Rhodamine 6G, are more than five and twelve times as toxic as KR620, respectively [7, 8], and also considered carcinogenic [1].

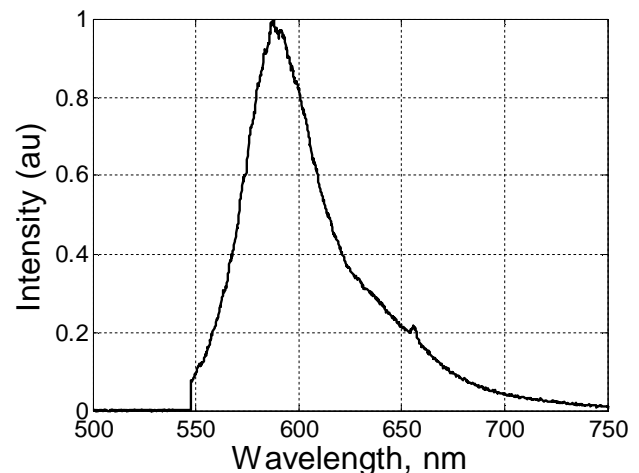


Figure 2.6. Measured emission spectrum of Kiton Red 620 doped PSLs collected from excitation with a continuous-wave laser at 532 nm. A spectral filter blocked the laser light.

2.4 PIV Processing Vector Validation

As described in Section 2.1, the correlation peak of an interrogation window is used to determine the displacement vector of the particles in that window. For images with weak signal or

excessive noise, there is a possibility that the correlation peak of an interrogation window is invalid (or “spurious”), and not reflective of the actual displacement of the particles. To gauge the quality of PIV data taken, validation rates of vectors in the velocity field were calculated. A general rule of thumb is to have at least 95% valid vectors in a given vector field [1]. In this study, spurious vectors were detected by first instituting a minimum peak ratio value for acceptance and then using a median filter.

The peak ratio Q , also referred to as “detectability” or “Primary Peak Ratio (PPR)” in the literature, is defined as the ratio of the highest to second highest displacement correlation peak for a given interrogation window [1, 9]:

$$Q \equiv \frac{\textit{Highest Correlation Peak Height}}{\textit{Second Highest Correlation Peak Height}} \quad (2.3)$$

All peak ratio calculations in this thesis measure the peak heights relative to the correlation noise floor. It has been generally accepted that a reasonable value for the minimum peak ratio threshold is 1.2 - 1.5, where vectors above this peak ratio are considered valid [10]. Other studies have shown that peak ratios above 2.0 are preferred for both spurious vector removal [11] and the lowest uncertainty in the calculated displacement [12].

The median filter was first introduced as a method for spurious vector removal by Westerweel [13] and later expanded upon by Westerweel and Scarano [14]. The median filter used for spurious vector removal in the following paper is based on the value of a normalized residual r , defined as

$$r = \frac{|\vec{U}_0 - \vec{U}_m|}{\sigma} \quad (2.4)$$

where \vec{U}_0 is the displacement vector of a given interrogation window, \vec{U}_m is the median displacement among the 8 neighboring vectors of the interrogation window of interest, and σ is the r.m.s. value of those neighboring vectors. When calculating σ , the displacements of the two most deviant neighbors are neglected to prevent neighboring spurious vectors from influencing the process. For all processing and validation described in this paper, a PIV vector was removed if its residual value, r , was greater than 2.

2.5 Preliminary Test Results

The first step in demonstrating fluorescent PIV using KR620 PSLs was to prove that the reduced fluorescence signal was sufficient for valid PIV data. The data shown in this section were taken using the experimental setup from Section 2.2.1.

Multiple sets of tests were run in the VTFD Lab on fluorescence PIV signal quality from the free jet, using the configuration detailed in Section 2.2.1 and Figure 2.3. Pictured in Figure 2.7 are raw single-shot images captured by the PIV camera showing the flow at the exit of the

nozzle exhaust. The top image was taken without the laser-blocking filter and shows the Mie scattered light. The bottom image was taken using the 560-nm long pass filter and therefore only contains fluorescent light emitted by the KR620 particles. The particles were originally estimated to be about 3 orders of magnitude brighter in the unfiltered Mie scattering images compared to the LIF images, which required different apertures to view the flow while holding laser illumination constant. Further investigation into the signal differences is presented in Section 3.4.1, which concluded that the signal difference in this configuration was actually a factor of 320.

Despite the lower signal, the overall flow instability is still clearly visible with the fluorescent light and results in a well-seeded image of the core jet flow. The flow is from right to left in these images. The diminished signal intensity in the right-hand side of the image in Figure 2.7b is caused by a reduced sensitivity of the right half of the sensor – an artifact of the experiment that is exacerbated by the lower signals in the fluorescent PIV images.

The image sets were processed using the DaVis software to obtain particle velocity vectors. The velocity maps obtained with Mie scattered data are plotted in Figure 2.8. The original image from Figure 2.8a, the processed U- and V- velocities (along the x- and y- axes as labeled in Figure 2.7), and the average U-velocity from a set of 15 such images are contained in this figure. The same four plots obtained using the fluorescent particle light are shown in Figure 2.9.

These initial test results lead to a few conclusions. First, the Mie and fluorescent processed images can successfully measure detailed flow features seen in the individual images. For example, the radial velocities expected from the ring-vortex instabilities seen in Figure 2.8a and Figure 2.9a can be clearly seen in both Figure 2.8c and Figure 2.9c. Second, and most importantly, the U-velocity average from the KR620 fluorescent images in Figure 2.9d is within 3% of the U-velocity average of the Mie scattered images at the nozzle exit.

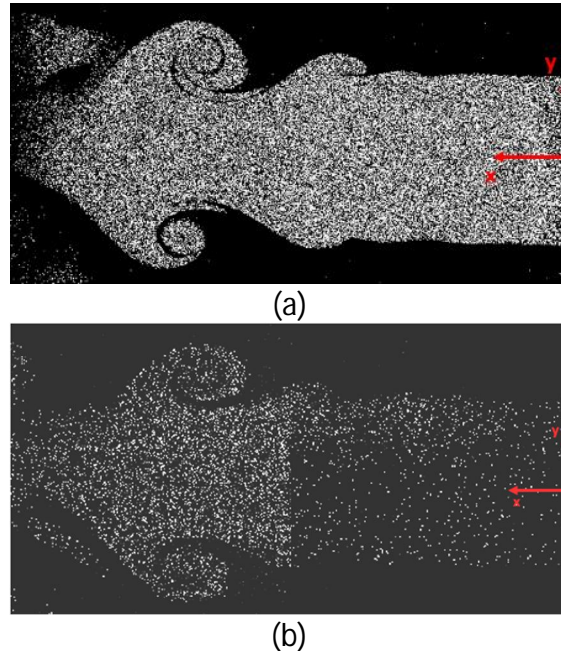
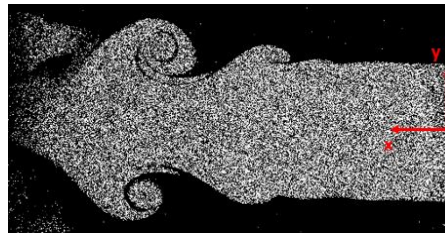
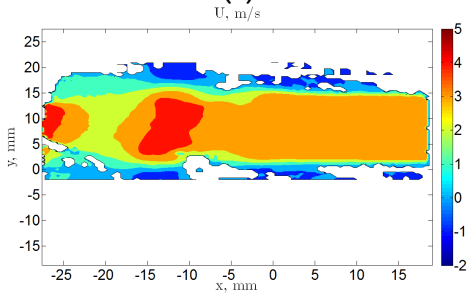


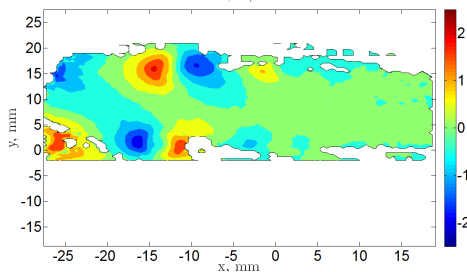
Figure 2.7. Camera images of Mie scattered light (a) and KR620 fluorescent light (b). Images were taken at a nozzle exit velocity of 3.5 m/s. The images were not taken simultaneously.



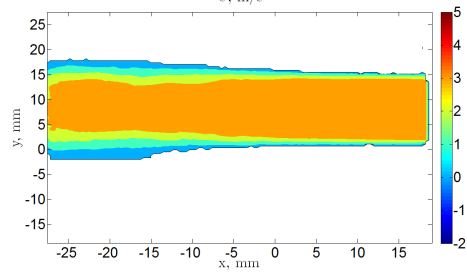
(a)



(b)

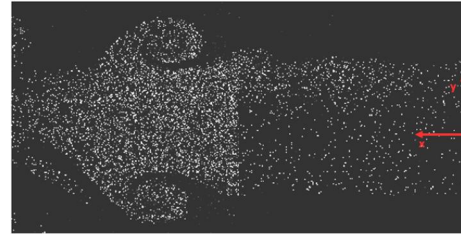


(c)

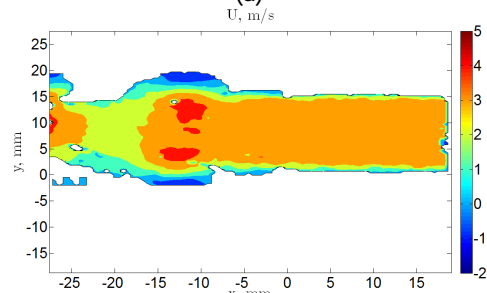


(d)

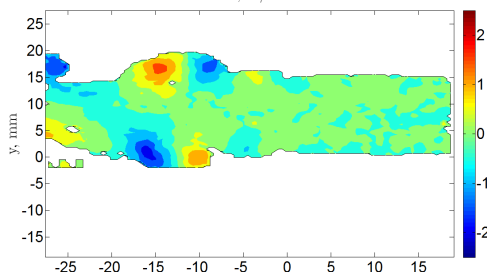
Figure 2.8. Original camera image of Mie scattered light (a), single image processed PIV data of U- and V- velocities (b and c), and 15 image average U- velocity (d).



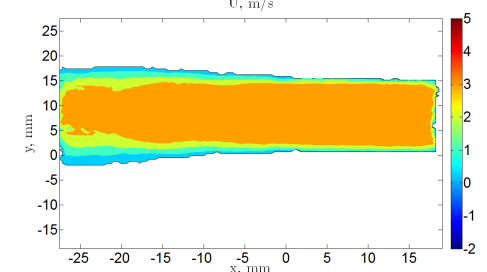
(a)



(b)



(c)



(d)

Figure 2.9. Original camera image of KR620 fluorescence (a), single image processed PIV data of U- and V- velocities (b and c), and 15 image average U- velocity (d).

Next, the average stream-wise velocity components across the nozzle exit were compared, as seen in Figure 2.10. Because the sets of images were taken back to back, rather than simultaneously, it is strongly believed that the slight difference is more indicative of nozzle unsteadiness than an instrumentation bias in PIV data from fluorescent images.

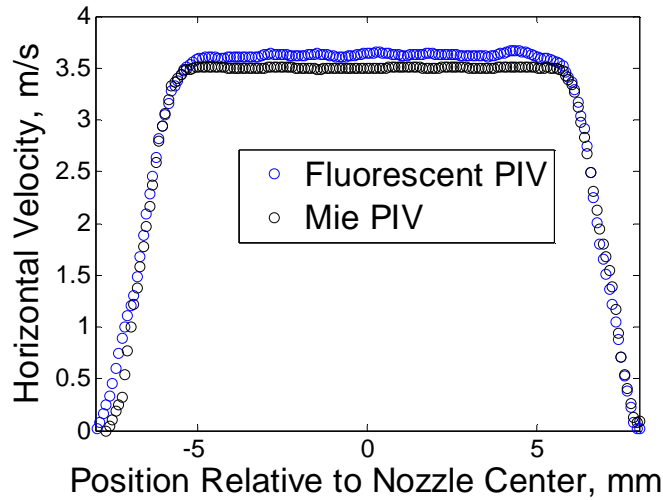


Figure 2.10. Stream-wise velocity averages across nozzle exit.

Another way to study the two image sets is to compare their validation rates. If the fluorescent PIV data validated at a low rate, it would be indicative that the fluorescent signal from the particles is too low for accurate velocimetry. Table 2.1 compares the validation rates from the two sets for a large region of the core jet flow across all of the images.

The results indicate that while the fluorescent PIV validation rates were lower than the corresponding Mie PIV rates, they far exceed the generally accepted standards for PIV. It can be concluded from these tests that the fluorescence signal from KR620 doped PSL microspheres is noticeably dimmer than the Mie-scattered light off of the particles, but still sufficient for PIV. The next steps would be to demonstrate PIV applications using fluorescent particles that wouldn't otherwise be possible using Mie-scattered light from the particles. This work is documented in Section 3.

Table 2.1. Vector validation rate comparison for benchtop fluorescent PIV.

Technique	Percent Valid, $Q > 1.3$
Fluorescence	98.2%
Mie	100%

2.6 References

- [1] Adrian R and Westerweel J, Particle Image Velocimetry, New York: Cambridge University Press, 2011.
- [2] Melling A, "Tracer Particles and Seeding for Particle Image Velocimetry," *Measurement Science and Technology*, vol. 8, no. 12, 1997.
- [3] DaVis Software Package, Ver. 8.2, LaVision, Goettingen, Germany, 2014.

- [4] Tiemsin P and Wohl C, "Refined Synthesis and Characterization of Controlled Diameter, Narrow Size Distribution Microparticles for Aerospace Research Applications," *NASA Technical Memorandum*, pp. TM-2012-217591, 2012.
- [5] Danehy P, Tiemsin P, Wohl C, Verkamp M, Lowe T, Maisto P, Byun G and Simpson R, "Fluorescence-Doped Particles for Simultaneous Temperature and Velocity Imaging," *NASA Technical Memorandum*, pp. TM-2012-217768, 2012.
- [6] Exciton, INC, "Material Safety Data Sheet- Kiton Red 620," 13 1 2004. [Online]. Available: http://www.indeco.jp/indeco_online/main/htm/msds/kr620.pdf.
- [7] ScienceLab.com, Inc., "Material Safety Data Sheet- Rhodamine B," 21 5 2013. [Online]. Available: <http://www.sciencelab.com/msds.php?msdsId=9924812>.
- [8] ScienceLab.com, Inc., "Material Safety Data Sheet- Rhodamine 6G," 21 5 2013. [Online]. Available: <http://www.sciencelab.com/msds.php?msdsId=9927579>.
- [9] Xue Z, Charonko J J and Vlachos P P, "Particle Image Velocimetry Correlation Signal-to-Noise Ratio Metrics and Measurement Uncertainty Quantification," *Measurement Science and Technology*, vol. 25, no. 11, 2014.
- [10] Keane R D and Adrian R J, "Optimization of Particle Image Velocimeters. I. Double Pulsed Systems," *Measurement Science and Technology*, vol. 1, no. 11, 1990.
- [11] Hain R and Kähler C J, "Fundamentals of Multiframe Particle Image Velocimetry (PIV)," *Experiments in Fluids*, vol. 42, no. 4, pp. 575-587, 2007.
- [12] Charonko J J and Vlachos P P, "Estimation of Uncertainty Bounds for Individual Particle Image Velocimetry Measurements from Cross-Correlation Peak Ratio," *Measurement Science and Technology*, vol. 24, no. 6, 2013.
- [13] Westerweel J, "Efficient Detection of Spurious Vectors in Particle Image Velocimetry Data," *Experiments in Fluids*, vol. 16, no. 3-4, pp. 236-247, 1994.
- [14] Westerweel J and Scarano F, "Universal Outlier Detection for PIV Data," *Experiments in Fluids*, vol. 39, no. 6, pp. 1096-1100, 2005.

3. Laser Flare Removal in Particle Image Velocimetry Using Fluorescent Dye-doped Particles

3.1 Abstract

Laser flare can often be a major issue in Particle Image Velocimetry (PIV) involving solid boundaries in the flow or a gas-liquid interface. The use of fluorescent light from dye-doped particles has been demonstrated in water applications, but reproducing the technique in an airflow is more difficult due to particle size constraints and safety concerns. The following work presents fluorescent Kiton Red 620 (KR620)-doped polystyrene latex microspheres as a solution to this issue. The particles are small and monodisperse, with a mean diameter of $0.87 \mu\text{m}$. Furthermore, the KR620 dye exhibits much lower toxicity than other common fluorescent dyes, and would be safe to use in large flow facilities. The fluorescent signal from the particles is measured on average to be 320 ± 10 times weaker than the Mie scattering signal from the particles. This reduction in signal is counterbalanced by greatly enhanced contrast via optical rejection of the incident laser wavelength. Fluorescent PIV with these particles is shown to eliminate laser flare near surfaces, in one case leading to 63 times fewer spurious velocity vectors than an optimized Mie scattering implementation in a region more than 5 mm from an angled surface.

3.2 Introduction

Particle Image Velocimetry (PIV) is one of the most widely used non-intrusive flow diagnostics tools. This imaging-based technique allows for accurate velocity measurements at any point in the flow illuminated by a laser sheet, and has had numerous applications in studying both laminar and turbulent flows [1].

In many PIV experiments, a solid boundary interacts with the flow, such as an airfoil or flow channel wall. When the laser light reaches the surface of these objects, light is reflected and creates glare on the images. This laser flare is detrimental because it decreases the signal to noise ratio (SNR) and saturates the sensor pixels. In many instances, pixel blooming can also occur around saturations when photoelectrons leak into neighboring pixels, further expanding the imaging area affected by flare. In general, data in the presence of a glare are of low quality, if usable at all. Similar challenges also arise in liquid-gas flows, where light is reflected and refracted at the interface [2].

Many of the solutions for surface flare reduction involve modifications of the surface itself, including black paint [3], anodized black treatments [4], and clear models that match the index of

refraction of the testing fluid [5]. Paterna et. al. [6] provide a good summary of the types of surface treatments that have been used for laser flare reduction, and concluded through tests of their own that the application of fluorescent paint onto the testing surface was the best method for reducing glare. This technique has been used in the past successfully by Konrath et. al. [7] using a Rhodamine B doped black paint. However, another application using a Rhodamine 6G fluorescent paint was unsuccessful in eliminating flare near the surface of the wing model being tested, where velocimetry data was unattainable within 5-10 mm of the surface [8].

The fluorescent paint technique is an example of laser induced fluorescence (LIF). The incident laser light, reflected light from surfaces, and Mie-scattered light from the seed particles all occur at the same wavelength. When a fluorescent dye is excited by incident laser light, it emits light that is red-shifted relative to the incident light—the Stokes shift [9]. An appropriate optical filter can then be used to either pass only the fluorescent light or the Mie scattered light.

An alternative approach to the experiments presented above involves fluorescent particles. One may utilize the LIF signal from these particles for a variety of applications, including simultaneous temperature and velocity measurements [10, 11] or multi-stream flow tagging, for instance [12]. In the majority of applications in air, PIV data are taken using the Mie scattered light from the seed particles, while LIF is utilized by a second camera to obtain flow temperatures [13, 14]. Using fluorescent light for PIV, rather than Mie scattering, has been used on the macro scale in water flows [15, 16] and has had numerous applications in microscale PIV [17, 18]. The technique is more difficult to implement in a gas flow, which requires much smaller particles and safe dyes due to inhalation concerns [19, 20]. Fluorescent seed has been used on a few occasions for PIV in two phase flows, such as fuel injection into air [12, 21, 22]. These experiments demonstrated the technique using seed particles as small as 1-5 μm [21], although the work by Towers et. al. reported difficulty imaging particles smaller than 4 μm [12]. Another past effort [23] in an air flow was successful and demonstrated the application of fluorescent particles for flare removal in PIV, but utilized potentially dangerous seed particles that required protective measures for use.

The fluorescent light from seed particles can generally be expected to be a few orders of magnitude lower than the light from Mie scattering. The work by Towers et. al. [12] measured the fluorescence signal from 4-5 μm diameter Rhodamine 640 particles at 60 times weaker than the Mie scattered light from the same particles. The differences can be expected to become even more pronounced for small particles, because Mie scattered light scales with the square of the particle diameter (d_m^2) while fluorescent light scales with the cube of particle diameter (d_m^3), assuming a uniform fluorescent dye distribution over the particle volume [24].

Much of the past work with fluorescent dye-doped particles has involved the use of phosphor particles containing rare earth elements or other harmful chemicals such as toluene or Rhodamine [25, 26, 27, 28]. These chemicals can be dangerous and are unsafe to users in large

flow facilities. The present work has the focus of finding and applying safe fluorescent dyes to dope seed particles that can be used for LIF and flow diagnostics, such as PIV or Laser Doppler Velocimetry (LDV). Past work has centered around Dichlorofluorescein (DCF) and Kiton Red 620 (KR620) as safe alternatives for LIF, with KR620 exhibiting promising results [2, 20, 29]. The following discussions cover details of fluorescence yield for the KR620 safe particles and report a comparative study of Mie-scattering and fluorescent PIV for near-surface measurements.

3.3 Methods

Details of the testing equipment and experimental approach can be found in the following section, including a characterization of the seed particles used for PIV testing and description of the methodology used to quantify validation rates of the fluorescent and Mie PIV techniques.

3.3.1 Kiton Red Polystyrene Latex Particles

A common type of seed particle that has been used for PIV measurements is Polystyrene Latex (PSL) microspheres [24]. Recent work at NASA Langley Research Center has refined the manufacturing techniques of these spherical microparticles to create a highly uniform and tunable size distribution on the order of $1\ \mu\text{m}$ [30]. The KR620-doped PSL particles used in the present work had a $0.87\ \mu\text{m}$ monodisperse diameter and were developed using an improved proprietary version compared to that initially described in [29], using an emulsion polymerization technique.

The fluorescence emission spectrum of the particles, after being atomized and dispersed in air, was measured by a Thorlabs CCS175 spectrometer (Figure 3.1). The peak fluorescence emissions occur within the wavelength range of 580 - 600 nm, such that a long pass filter with a cut-on wavelength between 532 nm and this range can be used to reject Mie scattering and only transmit fluorescent light.

The toxicity of KR620 is very low, making it a good candidate for use in large, open air applications. It falls in the lowest category of toxicity according to its Material Data Safety Sheet [31]. For comparison, two other common fluorescent dyes, Rhodamine B and Rhodamine 6G, are more than five and twelve times as toxic as KR620, respectively [32, 33], and also considered carcinogenic [24].

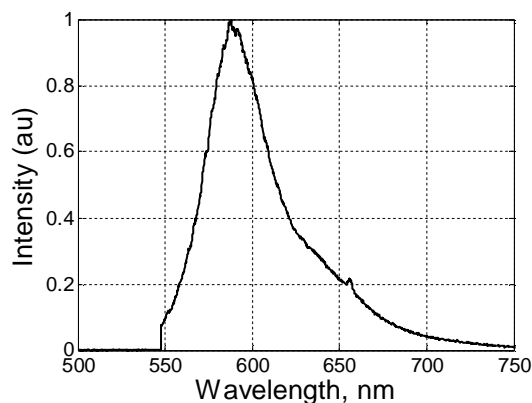


Figure 3.1. Measured emission spectrum of Kiton Red 620 doped PSLs collected from excitation with a continuous-wave laser at 532 nm. A spectral filter blocked the laser light.

3.3.2 Instrumentation and Experimental Setup

The PIV data included in this paper were recorded for the experimental setup seen in Figure 3.2. Tests used either one or two Photron SA1.1 Fastcam high-speed cameras with a 1024 x 1024 pixel resolution and 12-bit intensity digitization. The cameras were positioned above and below the airflow and perpendicular to the laser sheet for 2D PIV. Two Sigma 105 mm f/2.8 EX DG macro lenses were used with the cameras to obtain a close-up image of the flow. The camera fields of view were 30.7 x 30.7 mm² for single camera testing and 29.6 x 29.6 mm² for the two camera testing.

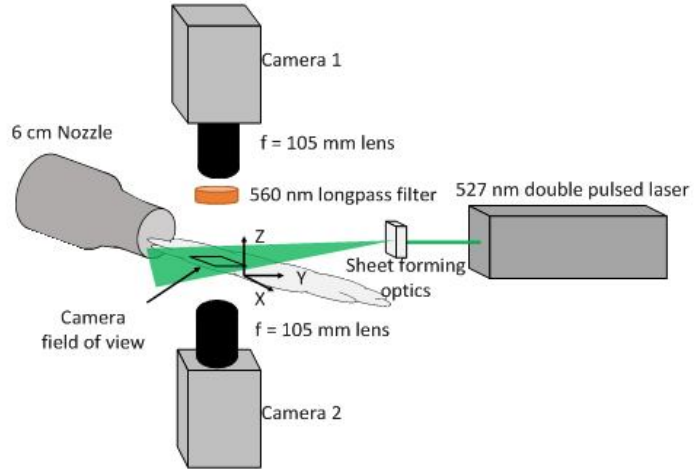


Figure 3.2. Experimental PIV test setup.

For fluorescence imaging, an Omega Optical 560 nm long pass filter, model 560HLP, was attached to the lens, blocking out all Mie scattered light from the particles and only allowing particle-emitted fluorescent light to be captured by the camera. A 527 nm dual-head Nd:YLF laser (Photonics Model DM30) was used at approximately 23 mJ/pulse to illuminate the flow and was controlled simultaneously with the camera by LaVision's DaVis software [34], recording at 2.5 kHz for time-resolved images. Finally, an $f = -20$ mm cylindrical lens was used to form a thin laser sheet at the nozzle exit in the orientation depicted in Figure 3.2. The laser sheet measured approximately 1.25 mm thick and 3.5 cm wide in the measurement plane at the nozzle exit. The cameras imaged a region of flow about 8 cm from the nozzle exit.

The KR620-doped PSL particles were seeded using two Air-o-Swiss 7146 ultrasonic humidifiers. Seed was introduced well upstream of the nozzle exit into the blower inlet, where it mixed with the air at room temperature and flowed through a nozzle of 6 cm exit diameter. The airflow at the exit for PIV tests was about 4.5 m/s, corresponding to a Reynolds number per meter of approximately 280,000 m⁻¹. Before each test, the KR620 particle solution was mixed in equal proportions with distilled water and sonicated for fifteen minutes in an L&R Quantrex 90H ultrasonic disruptor to prevent particle agglomeration. The mixture was then removed from the disruptor and placed immediately into the vaporizer.

The two camera setup seen in Figure 3.2 was used to image Mie scattered and fluorescent light simultaneously. Camera 2 was placed on a 3-axis traverse and 3-axis camera mount so that it

could be maneuvered to image the same particles in the flow. The results of this testing are provided in Section 3.4.1.

Additional tests were run with a single camera; the setup remained the same as seen in Figure 3.2 except for the removal of Camera 2. In these tests, the near-surface flow over a blunt leading edge flat aluminum plate was measured. In the first test, seen in Figure 3.3a, the plate was oriented parallel to the flow exiting the nozzle and perpendicular to the incident laser sheet. In the second test, seen in Figure 3.3b, the plate was oriented 45° to the incident laser sheet but still parallel to the airflow. The dimensions of the flat plate are shown in Figure 3.3c. For these single-camera tests, a set of 2000 double-frame fluorescent images was obtained with the filter over the lens. Then, the filter was quickly removed and another 2000 double-frame images were recorded of the Mie-scattered light from the seed particles.

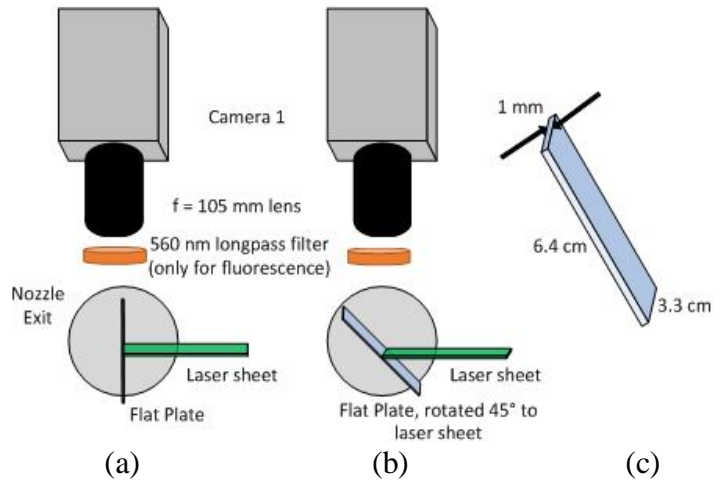


Figure 3.3. (a) Parallel flat plate orientation, (b) rotated plate orientation and (c) plate dimensions. Flow is out of the page.

3.3.3 PIV Processing Vector Validation

To gauge the quality of PIV data taken using the two techniques, the validation rates of vectors in the velocity field were compared. A general rule of thumb is to have at least 95% valid vectors in a given vector field [24]. In this study, spurious vectors were detected by first instituting a minimum peak ratio value for acceptance and then using a median filter. The peak ratio Q , also referred to as “detectability” or “Primary Peak Ratio (PPR)” in the literature, is defined as the ratio of the highest to second highest displacement correlation peak for a given interrogation window [24, 35]:

$$Q \equiv \frac{\text{Highest Correlation Peak Height}}{\text{Second Highest Correlation Peak Height}} \quad (3.1)$$

All peak ratio calculations in this paper measure the peak heights relative to the correlation noise floor. It has been generally accepted that a reasonable value for the minimum peak ratio threshold is 1.2 - 1.5, where vectors above this peak ratio are considered valid [36]. Other studies have shown that peak ratios above 2.0 are preferred for both spurious vector removal [37] and the lowest uncertainty in the calculated displacement [38]. For all data presented in the following paper, a peak ratio threshold of 1.3 was used. However, in the vector validation study, data were also processed with a peak ratio threshold of 2.0.

The median filter was first introduced as a method for spurious vector removal by Westerweel [39] and later expanded upon by Westerweel and Scarano [40]. The median filter used for spurious vector removal in the following paper is based on the value of a normalized residual r , defined as

$$r = \frac{|\vec{U}_0 - \vec{U}_m|}{\sigma} \quad (3.2)$$

where \vec{U}_0 is the displacement vector of a given interrogation window, \vec{U}_m is the median displacement among the 8 neighboring vectors of the interrogation window of interest, and σ is the r.m.s. value of those neighboring vectors. When calculating σ , the displacements of the two most deviant neighbors are neglected to prevent neighboring spurious vectors from influencing the process. For all processing and validation described in this paper, a PIV vector was removed if its residual value, r , was greater than 2.

3.4 Results

The experimental results are divided into two main sections. The first quantifies the signal differences between the fluorescent and Mie-scattered light from seed particles dispersed in an airflow. The second compares fluorescent PIV to Mie-scattered PIV for near-surface measurements.

3.4.1 Fluorescence and Mie Signal Characterization

Simultaneous Mie and fluorescence images were acquired for the KR620-doped PSL particles in order to directly compare their signal intensities. For these tests, the lens aperture of Camera 1 was set at $f/2.8$ to record fluorescent light, while the lens aperture of Camera 2 was at $f/22$ to record the brighter Mie-scattered light. The configuration for this test is shown in Figure 3.2. The nozzle was run at approximately 8 m/s, and a set of 2000 double-pulsed images was taken. After background subtraction, the images were compared. While the

same particle patterns were visible in both images, they did not overlap exactly due to small differences in camera alignment. To correct for this, image cross-correlation, analogous to that done for particle velocity processing, was computed from the fluorescent to Mie images. The resulting average displacement vector map, seen in Figure 3.4, shows a clear pattern indicating

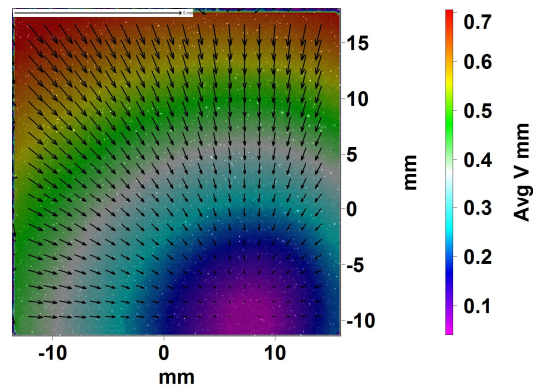


Figure 3.4. Fluorescence-to-Mie average image correlation map, indicating spatial mapping between cameras.

that the fluorescence camera has a slightly smaller field of view and is slightly shifted in the x- and y- directions relative to the Mie camera. The cross-correlation vector field was used to deform the fluorescent images using DaVis to obtain images that nearly exactly overlapped with the Mie images. A zoomed in view of a 50 x 50 pixel section of the resulting deformed simultaneous images is seen in Figure 3.5.

These simultaneous images can be beneficial in a number of ways. First, it allows for a clear look at the consistency of KR620 doping amongst the PSL particles. The expectation would be that for uniformly doped particles, the same relative particle intensities that appear in the Mie images would appear in the fluorescence images for monodisperse particles. However, as seen in Figure 3.5 (note particularly the particle in the upper left), this is not the case. While the majority of particles appear

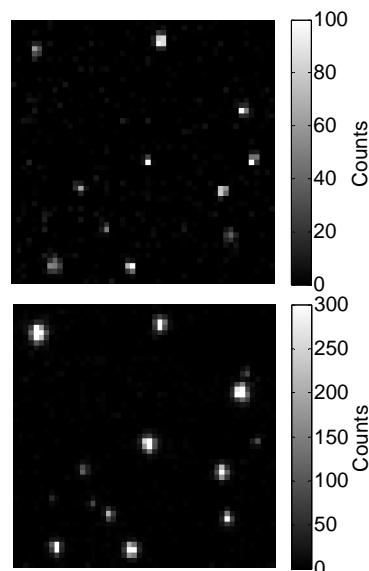


Figure 3.5. 50 x 50 pixel image of fluorescence image (above) and Mie-scattered image (below).

clearly in both Mie and fluorescence images, some exhibit almost no fluorescence. This suggests a degree of non-uniformity in the amount of dye contained in each particle. Whether this inconsistency originated from the original particle manufacturing process or occurred over time from dye leaching out of the particles is unknown and not the focus of the present paper. However, these images indicate that some improvements may be possible during the emulsion polymerization process to increase the amount of KR620 dye doped into each particle, which will serve to increase the fluorescent signal even further.

Because of the non-uniform particle doping, a single, absolute Mie-to-fluorescence signal ratio of the particles is not possible; however, a general estimate can be made. To characterize the signals, the images were broken up into square pixel bins. The signal was summed across all pixels in each fluorescence image bin and compared to the corresponding bin in the Mie images. An analysis of the background images indicated that random background camera noise stayed between 0-20 counts from pixel to pixel. In order to prevent noise from skewing the results, a minimum signal counts threshold was set, where all pixels under this threshold were set to 0 and discounted. Further, to ensure that the final results were accurate and not an artifact of the data processing technique, both the size of the pixel bins and the minimum signal threshold were varied. The areas of the image within 80 pixels of the edges were not included in the study to eliminate any edge effects from the image deformation process described earlier. 150 images from each technique were included in this study for a total of 48,000-438,000 bins, depending on the bin size. The Mie-to-fluorescence signal ratios from these bins were plotted in histogram format to determine the most common signal difference.

The amount of light entering the lens doubles as the aperture f-stop is decreased by one setting [41]. The Mie (f/22) and fluorescent (f/2.8) aperture settings are six f-stops apart, meaning that the fluorescent settings allow 2^6 times more light through the lens than the Mie images. Therefore, the total signal ratios are adjusted by a factor of 64.

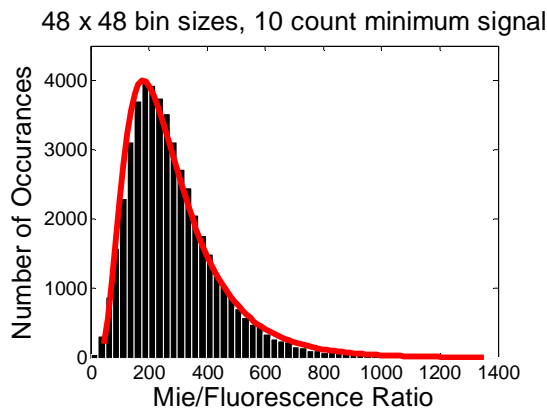


Figure 3.6. Mie to fluorescence particle signal ratios.

The histograms, such as the 48 x 48 bin result in Figure 3.6, show that the fluorescence yield from the particles is broad and skewed. This is due to the distribution of both particle sizes and the amount of dye doped in each particle. The ratios follow a log-normal distribution, which is also plotted in Figure 3.6. This indicates that a logarithmic detector is best for detecting the fluorescence signal. Previous studies have also found that fluorescent samples follow a log-normal distribution [42, 43].

With this knowledge, the signal ratio was quantified using the geometric mean and geometric standard deviation of the data. The data points in Figure 3.7 are the geometric mean of the signal ratios at the given pixel bin-count threshold combination, while the error bars correspond to one geometric standard deviation above or below the geometric mean.

The results from 24 x 24 pixel bin sizes and a 20 count threshold were chosen to be the truest indicators of the Mie/fluorescence ratio and particle to particle variation. While bin sizes did not heavily influence the geometric mean of the signal ratio, they did have an effect on the geometric standard deviation. The 24 x 24 bin size was chosen because the signal ratios coming from smaller bin sizes will be more representative of the ratio coming from a single particle. The 20 count signal threshold was chosen because at low count thresholds (5-10 counts), random noise from the cameras skew the results. Above 15 counts, the results even out. From this data, the overall ratio of Mie to fluorescent light from the particles is about 320 ± 10 , with an average particle's signal ratio expected to fall between 120 and 870- similar to that reported in a

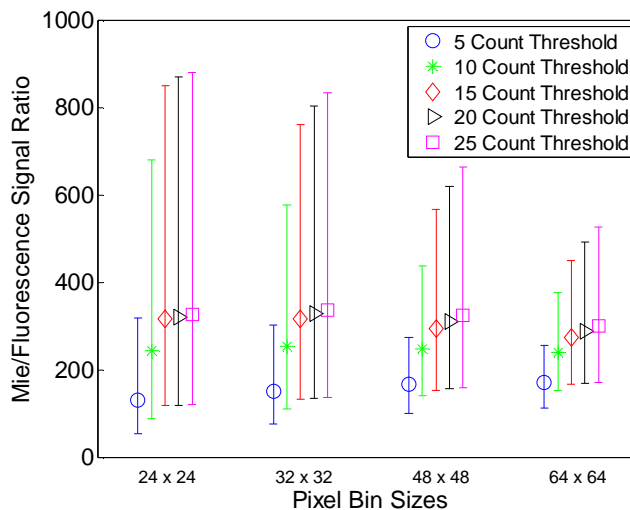


Figure 3.7. Mie to fluorescence particle signal ratios. The center point represents the geometric mean of the data set and error bars are one geometric standard deviation above and below the mean.

random noise from the cameras skew the results. Above 15 counts, the results even out. From this data, the overall ratio of Mie to fluorescent light from the particles is about 320 ± 10 , with an average particle's signal ratio expected to fall between 120 and 870- similar to that reported in a

previous study [12]. The geometric means of thirteen different data sets of 150 images were used in calculating the uncertainty in the average signal ratio, which represents a 95% confidence interval derived from a Student's t-distribution. These uncertainty bounds are within the marker sizes in Figure 3.7.

Quantification of the signal difference between the Mie-scattered and fluorescent light of micron sized particles is important for designing an experiment. For example, consider a standard PIV test of flow over an obstacle with a laser at 200 mJ/pulse forming a sheet 25 cm wide and 2 mm thick in the measurement plane. Assume Mie-scattering light off of particles could be recorded using a lens aperture of $f/22$. By adjusting the laser sheet dimensions to 5 cm wide by 1 mm thick and opening the lens aperture to $f/4$, the signal difference between Mie-scattering and fluorescent light from seed particles can be accounted for. Fluorescent PIV would generally only need to be used near surfaces, where laser flare is a major issue. In short, proper experimental planning with the appropriate camera lens and laser sheet optics can overcome any issues with fluorescent particle imaging, and the particles could be applied to any situation where Mie-scattering PIV is used.

3.4.2 Near-surface PIV

The first test with the flat plate used the configuration of Figure 3.3a, with the plate perpendicular to the laser sheet and camera directly above the sheet. First, a set of fluorescence images was taken with the lens aperture set at $f/2.8$. Then, the filter was removed and a set of Mie images was taken at $f/2.8$. Finally, another set of Mie images was taken with the aperture at $f/22$, where the signal from the particles roughly matched the signal from the fluorescence test. Example raw images from these tests are shown in Figure 3.8.

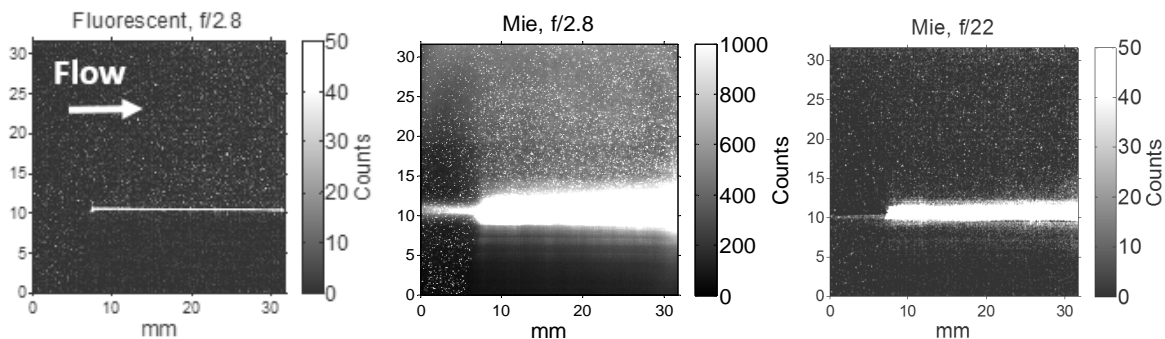


Figure 3.8. Flat plate camera images for (a) Fluorescent (left), (b) Mie $f/2.8$ (middle), and (c) Mie $f/22$ (right).

In this configuration, reflections from the flat plate should be at a minimum. However, as seen in Figure 3.8b and Figure 3.8c, there is considerable laser flare extending away from the plate surface. The plate surface is visible in Figure 3.8a for the fluorescence image because of a combination of particles stuck to the plate and Raman scattering and fluorescence from the aluminum surface.

Figure 3.9 presents another way of looking at the effects of laser flare. Plotted is the raw intensity signal from the three images in a line extending away from the plate surface at 50% chord. The plot shows that the camera is saturated near the plate surface for both Mie images. With the aperture at $f/2.8$, this region extends over 0.6 mm from the surface, and beyond that there is still a considerable background signal from laser flare that is 3 orders of magnitude higher than the random background noise seen in the fluorescent images. Closing the aperture to $f/22$ mitigates this to an extent, and the region of complete camera saturation only covers a few pixels away from the surface. However, the effects from laser flare are still seen up to 2 mm from the plate surface, with a background signal that is 1-3 orders of magnitude higher than the fluorescent images.

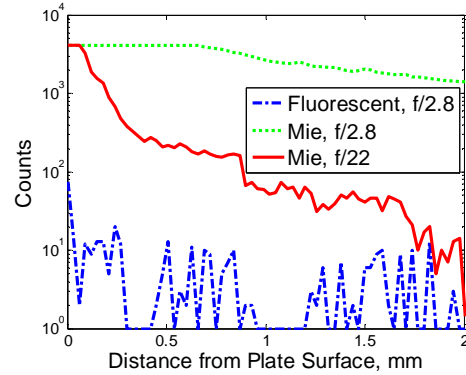


Figure 3.9. Background signal from laser flare.

The relative performance of fluorescence and Mie techniques was studied directly using PIV processing. After background subtraction, the images were processed using a multi-pass technique, with 64×64 pixel square interrogation windows and 50% overlap on the first pass and 24×24 pixel circular, Gaussian weighted interrogation windows on the second and third passes, with 87% overlap. Spurious vectors were removed via the methodology introduced in Section 3.3.3.

The resulting planar stream-wise velocity contours from the 2000 images are plotted in Figure 3.10, as are stream-wise velocity boundary layer profiles from 10% - 60% chord. The contour plots in Figure 3.10a-c cover the entire stream-wise field of view, and the region within 5 mm of the plate normal to the surface. The velocity contours for the three methods (Figure 3.10a-c) appear similar throughout most of the freestream flow. However, studying the velocities near the surface of the plate tell a different story.

The profiles from the fluorescent images in Figure 3.10d follow the expected trends for a laminar boundary layer developing on the plate. Velocities approach 0 m/s at the plate surface, and the boundary layer grows as flow progresses down the chord. The profile from the equivalent Mie data in Figure 3.10e is drastically different. Within 1-2 mm of the surface, the velocity values diverge from the fluorescent result and are calculated at 2-4 m/s at the apparent plate surface. Closing the lens aperture to $f/22$ does help significantly, as seen in Figure 3.10f. However, velocity values at the surface are still calculated to be 0.5-1 m/s between 20% and 60% chord positions.

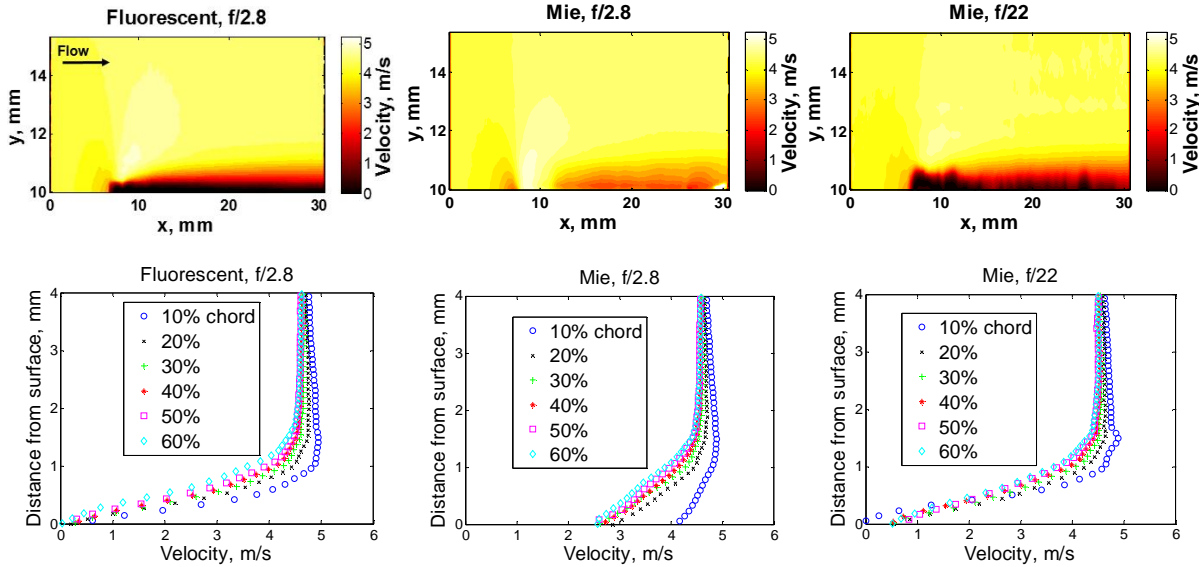


Figure 3.10. Flat plate processing results at top for (a) Fluorescent (left), (b) Mie f/2.8 (center), and (c) Mie f/22 (right). Contour plots cover the area within 5 mm from the plate surface. Corresponding boundary layer velocity profiles for (d) Fluorescent, (e) Mie f/2.8, and (f) Mie f/22.

The results from Figure 10d-f show a nonuniform freestream flow velocity that is indicative of an adverse pressure gradient. Therefore, the PIV profiles were compared to a Falkner-Skan profile, which is a boundary layer solution for laminar, incompressible flow over a wedge or angled plate subject to a pressure gradient [44]. Falkner-Skan solutions characterize the adverse pressure gradient through a term, β , which can be calculated from the freestream velocity profile using Equation 3.3:

$$u_e(x) = C * x^{\frac{\beta}{2-\beta}} \quad (3.3)$$

Using the freestream flow velocities from Figure 3.10d, a curve of the form in Equation 3.3 was fit, resulting in $\beta = -0.11$. The PIV data at 40%, 50%, and 60% chord are plotted in Figure 3.11 with the corresponding Falkner-Skan solution for comparison.

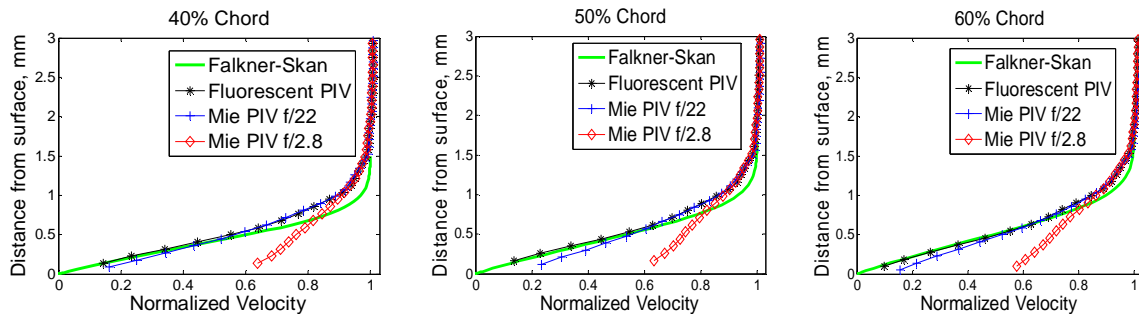


Figure 3.11. Falkner-Skan boundary layer profile comparison at (a) 40% chord (left), (b) 50% chord (middle), and (c) 60% chord (right).

These plots show that the Mie data at a lens aperture of $f/2.8$ is accurate until about 1.1 mm from the plate surface. The Mie data at an aperture of $f/22$ follows the boundary layer profile until about 0.5 mm from the surface, where it begins to diverge from the fluorescent and Falkner-Skan solution. The Falker-Skan and fluorescent data match to the plate surface.

From Figure 3.11, it can be seen that the laser flare skewed the processing results so that higher velocities were estimated through the boundary layer than what should be expected. This was an artifact of signal-to-noise ratio biasing for particles in the interrogation window that are farthest from flare of the plate surface. Due to the velocity gradient, these particles positively bias the result.

We conclude from these results that the fluorescent PIV technique allows for accurate velocimetry throughout the entire boundary layer, down to the plate surface. By comparison, a test at the same lens aperture using Mie scattered light was inaccurate within 1.0 mm of the plate surface. Closing the aperture to the point where the Mie signal roughly matched the fluorescence signal reduced the amount of laser flare, but still was inaccurate within 0.5 mm of the plate surface. Further, it is clear from the unsmooth contours of Figure 3.10b and Figure 3.10c that the small aperture resulted in fewer valid vectors from which to compute statistics.

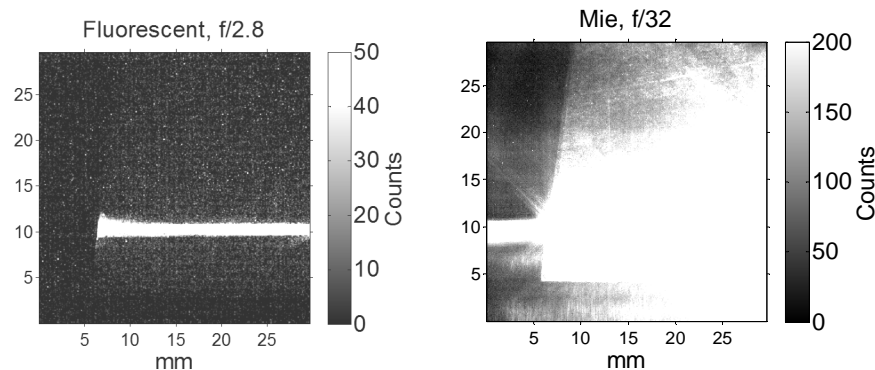


Figure 3.12. PIV images of (a) fluorescent particles (left) and (b) Mie particles (right).

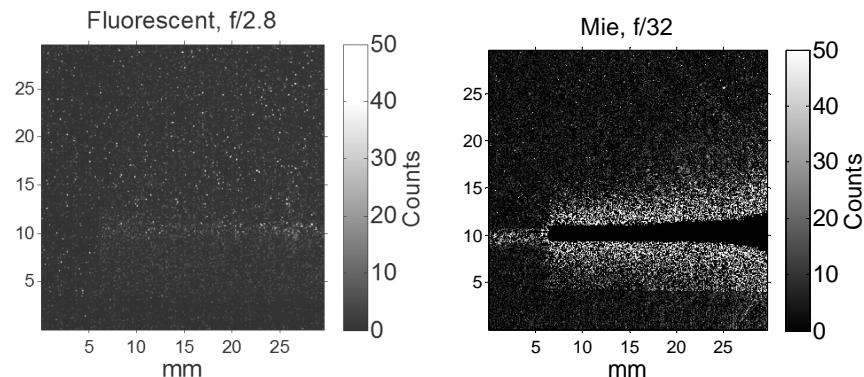


Figure 3.13. PIV images of (a) fluorescent particles (left) and (b) Mie particles (right) after background subtraction.

If PIV data are to be taken with an object of complex geometry in the flow, such as a rotor blade or airplane model, there will be instances where the object surface is at an angle to both the

incident light sheet and the imaging camera. In this case, laser flare from reflected light off of the complex surface may cause significant camera saturation and signal noise. To examine the degree to which this occurs, the flat plate tests were repeated with the plate rotated approximately 45° to the incident laser sheet and PIV camera, as illustrated in Figure 3.3b. Note that the camera is still perpendicular to the laser sheet. All other test conditions were the same as above except that the lens aperture for the Mie scattering images was closed to $f/32$. The aperture for fluorescence images remained at $f/2.8$.

Raw camera images for the two techniques can be seen in Figure 3.12, with the corresponding images after background subtraction in Figure 3.13. A brief examination of Figure 3.12b indicates that the majority of the Mie-scattering image contains background noise due to laser flare that extends far away from the plate, and particles are only visible at the top left corner of the image. A background subtraction cannot completely remove the effects of this laser flare, and seed particles can only be clearly seen on the outer edges of the image, where flare influence was least prominent.

The fluorescent images are strikingly different. The raw image from Figure 3.12a clearly shows seed particles throughout the image. Just as in the PIV viewed parallel to the surface, the strip where the laser sheet strikes the plate surface is visible in the fluorescent images due to a combination of Raman scattering and fluorescence. The sheet appears thicker in the image due to the plate rotation relative to the sheet. However, background subtraction is able to eliminate most of this noise while leaving the signals from moving particles unchanged.

To quantify and compare the background flare level, the raw pixel counts were extracted normal to the plate at the 50% chord location for both fluorescent and Mie images (Figure 3.14). The Mie image is completely saturated almost 1 mm away from the plate surface and remains 2-3 orders of magnitude higher in flare background than the fluorescent image.

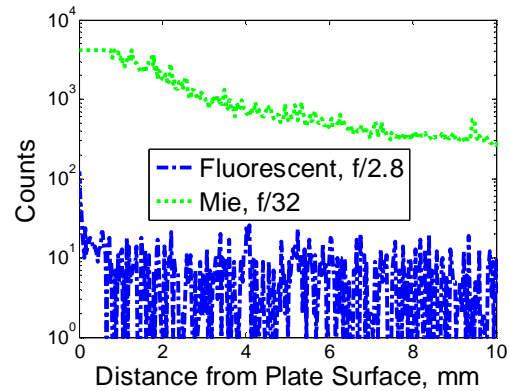


Figure 3.14. Background signal from laser flare for angled flat plate.

The image sets of 2000 images were processed in DaVis after background subtraction using a multi-pass technique with 32 x 32 pixel final pass interrogation windows, 87% overlap, and a median filter and $Q = 1.3$ peak ratio threshold for elimination of spurious vectors. The resulting average stream-wise velocity fields above the plate surface are shown in Figure 3.15, which include only the vectors from the 2000 images that passed the validation requirements. The average velocity obtained from fluorescence images qualitatively matches the results presented in Figure 3.10a, while the results from the Mie images are clearly erroneous within 5-10 mm of the surface.

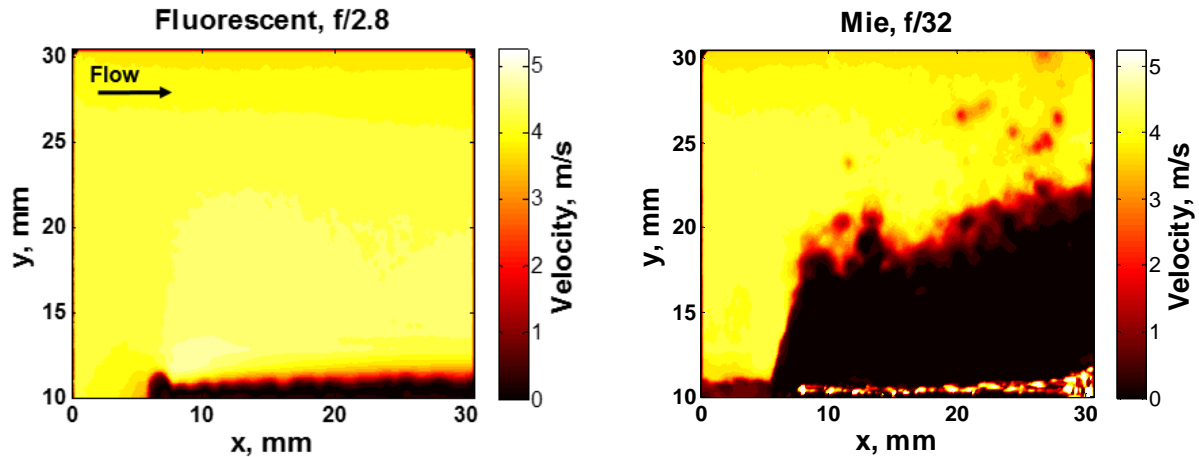


Figure 3.15. Angled flat plate processing results for (a) Fluorescent PIV f/2.8 (left), (b) Mie PIV f/32 (right).

To further quantify the performance of the fluorescent PIV, the validation rates from a 25 x 18 mm² region (4 mm x <math>< 29</math> mm, 11.5 mm y <math>< 29.5</math> mm in Figure 3.15) above the plate in the free stream flow were compared across 100 images. This region enclosed over 3.5 million possible valid vectors across the 100 images. A vector was considered valid if it both passed the requirements described in section 2.3 and had a velocity component parallel to the plate between 2 and 7 m/s (expected range for the 4.5 m/s freestream flow).

The results were compared for peak ratio thresholds of 1.3 and 2 in Table 3.1. The data in Table 3.1 indicate that for a peak ratio threshold of 1.3, which is standard for PIV, there were over 63 times as many invalid vectors using Mie scattered light compared to fluorescent. The validation rates of the Mie images fall well short of the standard rule of thumb of 95%, and, as is immediately evident upon examining the contours of Figure 3.15b, the processed vector fields are unreliable. The fluorescent images, on the other hand, validate well above 95%. Measurements within the diffraction-limited particle image are feasible using fluorescent light with the application of particle tracking algorithms.

Table 3.1. Vector validation rate comparison.

Technique	Percent Valid, $Q > 1.3$	Percent Valid, $Q > 2$
Fluorescence	99.0%	95.1%
Mie	36.6%	24.7%

3.5 Conclusions

In many PIV applications, laser flare from solid surfaces or gas-liquid interfaces leads to camera saturation and low signal-to-noise ratio. As a result, velocity vectors cannot be obtained in these regions. A promising technique for flare reduction is imaging laser induced fluorescence from fluorescent particles. An optical filter can be used to reject incident laser light surface reflection from objects or boundaries in the flow and only image the fluorescent light from seed particles.

The current application of Kiton Red 620-doped polystyrene latex spheres (PSLs) of 0.87 μm monodisperse diameter is the first known to the authors which combines important requirements for airborne applications—safety and micrometer size. The particles and dye have much lower toxicity than other common fluorescent dyes used in LIF applications, and would be safe enough for usage in a large, open facility or wind tunnel. The overall fluorescent signal was measured to be 320 ± 10 times weaker than the Mie scattering from the seed particles with the signal difference of most particles falling within the 120 and 870 range. This test used two-camera imaging that simultaneously captured Mie and LIF signals from large ensembles of the same particles.

The results presented validate the fluorescent PIV method for very small, doped PSL particles dispersed in air flows. Fluorescent PIV was used to measure the boundary layer flow over a flat plate. The double-pulsed fluorescent images were cross-correlated to obtain velocity measurements of the flow all the way down to the plate surface. In contrast, the same experiment using Mie-scattered light yielded invalid measurements within 1 mm of the surface due to laser flare. Closing the lens aperture did improve the Mie PIV, but in the best case valid velocity vectors were available at distances greater than 500 μm from the plate surface.

In real-world applications, it is often not possible to image a surface flow at a grazing angle. A simple representation of this case was produced by orienting the plate at a 45° angle to both the incident laser sheet and camera. Using fluorescent PIV in this configuration led to 63 times fewer spurious vectors than Mie PIV, which was unable to correlate particles within 5-10 mm of the plate due to laser flare. This quantifies the potential of the safe fluorescent particles for use in many flow measurements that would not otherwise be possible.

3.6 Acknowledgements

The authors acknowledge the support of the NASA ARMD Seedling Fund and NIA Cooperative Agreement NNL09AA00A.

3.7 References

- [1] Adrian R J, "Twenty Years of Particle Image Velocimetry," *Experiments in Fluids*, vol. 39, no. 2, pp. 159-169, 2005.
- [2] Petrosky B, Maisto P, Lowe K T, André M, Bardet P, Tiemsin P, Wohl C and Danehy P, "Particle Image Velocimetry Applications Using Fluorescent Dye-doped Particles," in *AIAA Scitech*, Kissimmee, 2015.
- [3] Wernet M P, "Development of Digital Particle Imaging Velocimetry for Use in Turbomachinery," *Experiments in Fluids*, vol. 28, no. 2, pp. 97-115, 2000.
- [4] Rostamy N, Sumner D, Bergstrom D J and Bugg J D, "Local Flow Field of a Surface-Mounted Finite Circular Cylinder," *Journal of Fluids and Structures*, vol. 34, pp. 105-122, 2012.
- [5] Uzol O, Chow Y C, Katz J and Meneveau C, "Unobstructed Particle Image Velocimetry Measurements within an Axial Turbo-pump Using Liquid and Blade with Matched Refractive Indices," *Experiments in Fluids*, vol. 33, no. 6, pp. 909-919, 2002.
- [6] Paterna E, Moonen P, Dorer V and Carmeliet J, "Mitigation of Surface Reflection in PIV Measurements," *Measurement Science and Technology*, vol. 24, no. 5, 2013.
- [7] Konrath R, Klein C, Schröder A and Kompenhans J, "Combined Application of Pressure Sensitive Paint and Particle Image Velocimetry to the Flow Above a Delta Wing," *Experiments in Fluids*, vol. 44, no. 3, pp. 357-366, 2007.
- [8] Watanabe S, Kato H, Kwak D, Shirotake M and Rinoie K, "Stereoscopic PIV Measurements of Leading Edge Separation Vortices on a Cranked Arrow Wing," *Measurement Science and Technology*, vol. 15, no. 6, 2004.
- [9] Lakowicz J R, Principles of Fluorescence Spectroscopy, New York: Springer Science & Business Media, 2007.
- [10] Peterson B, Baum E, Böhm B, Sick V and Dreizler A, "Evaluation of Toluene LIF Thermometry Detection Strategies Applied in an Internal Combustion Engine," *Applied Physics B*, vol. 117, no. 1, pp. 151-175, 2014.
- [11] Abram C, Fond B, Heyes A and Beyrau F, "High-speed Planar Thermometry and Velocimetry Using Thermographic Phosphor Particles," *Applied Physics B*, vol. 111, no. 2, pp. 115-160, 2013.
- [12] Towers D P, Towers C E, Buckberry C H and Reeves M, "A Colour PIV System Employing Fluorescent Particles for Two-Phase Flow Measurements," *Measurement Science and Technology*, vol. 10, no. 9, 1999.
- [13] Hishida K and Sakakibara J, "Combined Planar Laser-induced Fluorescence- Particle Image Velocimetry Technique for Velocity and Temperature Fields," *Experiments in Fluids*, vol. 29, no. 1, pp. S129-S140, 2000.
- [14] Carter C D, Donbar J M and Driscoll J F, "Simultaneous CH Planar Laser-induced Fluorescence and Particle Imaging Velocimetry in Turbulent Nonpremixed Flames," *Applied Physics B*, vol. 66, no. 1, pp. 129-132, 1998.
- [15] Poussou S and Plesniak M W, "Near-Field Flow Measurements of a Cavitating Jet Emanating From a Crown-Shaped Nozzle," *Journal of Fluids Engineering*, vol. 129, no. 5, 2006.
- [16] Lozano A, Barreras F, Fueyo N and Santodomingo S, "The Flow in an Oil/Water Plate Heat Exchanger for the Automotive Industry," *Applied Thermal Engineering*, vol. 28, no. 10, pp. 1109-1117, 2008.
- [17] Wereley S and Meinhart C D, "Recent Advances in Micro-Particle Image Velocimetry," *Annual Review of Fluid Mechanics*, vol. 42, pp. 557-576, 2010.
- [18] Singh A K, Cummings E B and Throckmorton D J, "Fluorescent Liposome Flow Markers for Microscale Particle-Image Velocimetry," *Analytical Chemistry*, vol. 73, no. 5, pp. 1057-1061, 2001.

- [19] Lowe K T, Maisto P, Byun G, Simpson R, Verkamp M, Danehy P, Tiemsin P and Wohl C, "Laser Velocimetry with Fluorescent Dye-Doped Polystyrene Microspheres," *Optics Letters*, vol. 38, no. 8, pp. 1197-1199, 2013.
- [20] Maisto P, Lowe K T, Byun G, Simpson R, Verkamp M, Danley J, Koh B, Tiemsin P, Danehy P and Wohl C, "Characterization of Fluorescent Polystyrene Microspheres for Advanced Flow Diagnostics," in *AIAA AMT Conference*, San Diego, 2013.
- [21] Kosiwczuk W, Cessou A, Trinité M and Lecordier B, "Simultaneous Velocity Field Measurements in Two-Phase Flows for Turbulent Mixing of Sprays by Means of Two-Phase PIV," *Experiments in Fluids*, vol. 39, no. 5, pp. 895-908, 2005.
- [22] Driscoll K D, Sick V and Gray C, "Simultaneous Air/Fuel-Phase PIV Measurements in a Dense Fuel Spray," *Experiments in Fluids*, vol. 35, no. 1, pp. 112-115, 2003.
- [23] Chennaoui M, Angarita-Jaimes D, Ormsby M P, Angarita-Jaimes N, McGhee E, Towers C E, Jones A C and Towers D P, "Optimization and Evaluation of Fluorescent Tracers for Flare Removal in Gas-Phase Particle Image Velocimetry," *Measurement Science and Technology*, vol. 19, no. 11, 2008.
- [24] Adrian R and Westerweel J, *Particle Image Velocimetry*, New York: Cambridge University Press, 2011.
- [25] Omrane A, Petersson P, Aldén M and Linne M A, "Simultaneous 2D Flow Velocity and Gas Temperature Measurements Using Thermographic Phosphors," *Applied Physics B*, vol. 92, no. 1, pp. 99-102, 2008.
- [26] Brübach J, Patt A and Dreizler A, "Spray Thermometry Using Thermographic Phosphors," *Applied Physics B*, vol. 83, no. 4, pp. 499-502, 2006.
- [27] Omrane A, Särner G and Aldén M, "2D-temperature Imaging of Single Droplets and Sprays Using Thermographic Phosphors," *Applied Physics B*, vol. 79, no. 4, pp. 431-434, 2004.
- [28] Rottenkolber G, Gindele J, Raposo J, Dullenkopf K, Hentschel W, Wittig S, Spicher U and Merzkirch W, "Spray Analysis of a Gasoline Direct Injector by Means of Two-Phase PIV," *Experiments in Fluids*, vol. 32, no. 6, pp. 710-721, 2002.
- [29] Danehy P, Tiemsin P, Wohl C, Verkamp M, Lowe T, Maisto P, Byun G and Simpson R, "Fluorescence-Doped Particles for Simultaneous Temperature and Velocity Imaging," *NASA Technical Memorandum*, pp. TM-2012-217768, 2012.
- [30] Tiemsin P and Wohl C, "Refined Synthesis and Characterization of Controlled Diameter, Narrow Size Distribution Microparticles for Aerospace Research Applications," *NASA Technical Memorandum*, pp. TM-2012-217591, 2012.
- [31] Exciton, INC, "Material Safety Data Sheet- Kiton Red 620," 13 1 2004. [Online]. Available: http://www.indeco.jp/indeco_online/main/htm/msds/kr620.pdf.
- [32] ScienceLab.com, Inc., "Material Safety Data Sheet- Rhodamine B," 21 5 2013. [Online]. Available: <http://www.sciencelab.com/msds.php?msdsId=9924812>.
- [33] ScienceLab.com, Inc., "Material Safety Data Sheet- Rhodamine 6G," 21 5 2013. [Online]. Available: <http://www.sciencelab.com/msds.php?msdsId=9927579>.
- [34] DaVis Software Package, Ver. 8.2, LaVision, Goettingen, Germany, 2014.
- [35] Xue Z, Charonko J J and Vlachos P P, "Particle Image Velocimetry Correlation Signal-to-Noise Ratio Metrics and Measurement Uncertainty Quantification," *Measurement Science and Technology*, vol. 25, no. 11, 2014.

- [36] Keane R D and Adrian R J, "Optimization of Particle Image Velocimeters. I. Double Pulsed Systems," *Measurement Science and Technology*, vol. 1, no. 11, 1990.
- [37] Hain R and Kähler C J, "Fundamentals of Multiframe Particle Image Velocimetry (PIV)," *Experiments in Fluids*, vol. 42, no. 4, pp. 575-587, 2007.
- [38] Charonko J J and Vlachos P P, "Estimation of Uncertainty Bounds for Individual Particle Image Velocimetry Measurements from Cross-Correlation Peak Ratio," *Measurement Science and Technology*, vol. 24, no. 6, 2013.
- [39] Westerweel J, "Efficient Detection of Spurious Vectors in Particle Image Velocimetry Data," *Experiments in Fluids*, vol. 16, no. 3-4, pp. 236-247, 1994.
- [40] Westerweel J and Scarano F, "Universal Outlier Detection for PIV Data," *Experiments in Fluids*, vol. 39, no. 6, pp. 1096-1100, 2005.
- [41] Birn J, *Digital Lighting and Rendering*, New Riders, 2014.
- [42] Campbell J W, "The Lognormal Distribution as a Model for Bio-Optical Variability in the Sea," *Journal of Geophysical Research*, vol. 100, no. C7, pp. 13,237-13,254, 1995.
- [43] Furusawa C, Suzuki T, Kashiwagi A, Yomo T and Kaneko K, "Ubiquity of Log-Normal Distributions in Intra-Cellular Reaction Dynamics," *Biophysics*, vol. 1, pp. 25-31, 2005.
- [44] Schetz J A and Bowersox R, *Boundary Layer Analysis*, Reston: American Institute of Aeronautics and Astronautics, 2011.

4. Final PIV Conclusions

In many PIV applications, laser flare from solid surfaces or gas-liquid interfaces leads to regions of camera saturation and low signal-to-noise ratio. As a result, velocity vectors cannot be obtained in these regions. Surface treatments are available to reduce reflections, but they are ineffective, expensive, or contain hazardous materials. However, a promising technique for flare reduction is imaging laser induced fluorescence from fluorescent particles. Through the Stokes shift, an optical filter can be used to reject incident laser light surface reflection from objects or boundaries in the flow and only image the fluorescent light from seed particles.

The current application uses Kiton Red 620-doped polystyrene latex spheres (PSLs) of 0.87 μm monodisperse diameter. The particles and dye have much lower toxicity than other common fluorescent dyes used in LIF applications, and would be safe for usage in a large, open facility or wind tunnel. The results presented in Section 2 validate the fluorescent PIV method for very small, doped PSL particles dispersed in air flows. In these tests, PIV data was taken of a free jet flow using both fluorescent and Mie-scattered light. The results showed that the reduced signal from the fluorescent particles was still sufficient for taking PIV measurements.

In Section 3, the overall fluorescent signal was measured to be 320 ± 10 times weaker than the Mie scattering from the seed particles with the signal difference of most particles falling within the 120 and 870 range. This test used two-camera imaging that simultaneously captured Mie and LIF signals from large ensembles of the same particles. Next, fluorescent PIV was used to measure the boundary layer flow over a flat plate. The double-pulsed fluorescent images were cross-correlated to obtain velocity measurements of the flow all the way down to the plate surface. In contrast, the same experiment using Mie-scattered light yielded invalid measurements within 1 mm of the surface due to laser flare. Closing the lens aperture did improve the Mie PIV, but in the best case valid velocity vectors were available at distances greater than 500 μm from the plate surface.

In real-world applications, it is often not possible to image a surface flow at a grazing angle. A simple representation of this case was produced by orienting the plate at a 45° angle to both the incident laser sheet and camera. Using fluorescent PIV in this configuration led to 63 times fewer spurious vectors than Mie PIV, which was unable to correlate particles within 5-10 mm of the plate due to laser flare.

The current application of Kiton Red 620-doped polystyrene latex spheres (PSLs) of 0.87 μm monodisperse diameter is the first known to the authors which combines important requirements for airborne fluorescent PIV applications—safety and micrometer size. The particles and dye have much lower toxicity than other common fluorescent dyes used in LIF applications, and would be safe enough for usage in a large, open facility or wind tunnel.

Furthermore, this research is also among the first to quantify a Mie-to-fluorescence signal ratio using simultaneous imaging of Mie-scattered and fluorescent light from particles in a flow. Quantification of the expected signal difference is important in the future design of experiments that will utilize fluorescent particles. The overall signal difference of the particles in the current work can be easily overcome with the proper optics and lenses. Future improvements in the particle dye-doping techniques can reduce this number even further. This research has demonstrated some of the many potential applications and benefits of fluorescent PIV and Kiton Red 620-doped PSLs. The work shows the potential of using safe fluorescent particles for flow measurements that would not otherwise be possible.

A. Appendix A: Kiton Red Thermometry

An additional study was done into using the Kiton Red 620 PSL particles for temperature measurements. The following sections detail the theory, relevant works, and initial experimental results for this work.

A.1 Introduction

Fluorescent dyes, excited through Laser Induced Fluorescence (LIF), have often been used as a temperature sensor because temperature can affect both the overall magnitude and shape of the fluorescence emission spectrum [1]. In many instances, the LIF signal from fluorescent particles has been used for temperature measurements, while light from Mie-scattering off of the particles has been used for PIV in simultaneous temperature and velocity measurements [2, 3].

Many experiments calculate temperature based on the ratio of total fluorescence signal in two distinct wavelength bands [4, 5]. The complete derivation can be found in [6, 7] and sources therein, but the essential equations are summarized below.

The total measured fluorescence signal in a region is the integral of the signal between its upper and lower wavelength bounds $\lambda_{i,1}$ and $\lambda_{i,2}$, and is given by:

$$I_{f,i} = \int_{\lambda_{i,1}}^{\lambda_{i,2}} I_1 c V K_{opt}(\lambda) K_{spec}(\lambda) e^{\left(\frac{\beta(\lambda)}{T}\right)} d\lambda \quad (\text{A.1})$$

In Equation A.1, I_1 is the incident laser intensity, c is the dye concentration, V is the measurement volume, $K_{opt}(\lambda)$ is an optical constant, $K_{spec}(\lambda)$ is a constant describing the spectral properties of the fluorescent dye, and $\frac{\beta(\lambda)}{T}$ describes the temperature dependence of the dye.

Equation A.1 has been shown to be approximated by:

$$I_{f,i} \approx I_1 c V K_{opt,i}(\lambda) K_{spec,i}(\lambda) e^{\left(\frac{A_i + B_i}{T^2 + T} + C_i\right)} \quad (\text{A.2})$$

Where A_i , B_i , and C_i are constants describing the shape of the curve. Equation A.2 leaves a lot of terms to be solved for in an experiment. However, by using two wavelength bands of the same dye and taking a ratio between the total signal in each, nearly all of the constants cancel out and the only factor left is the temperature dependence. Assuming the signal from both wavelength bands is recorded using optical systems with identical properties, this ratio becomes:

$$R_f(T) = \frac{I_{B_2}}{I_{B_1}} = e^{\left(\frac{A}{T^2 + T} + C\right)} \quad (\text{A.3})$$

The first step in using LIF for temperature measurements is to calibrate the signal, where the two-band signal ratio is calculated at known temperatures, and a curve of the form in Equation A.3 is fit to the results. The sections below describe an experiment to generate a

calibration curve for the fluorescence temperature dependence of Kiton Red 620 doped PSLs in an airflow.

A.2 Calibration Experiment Setup

The test configuration used for the temperature experiments is seen in Figure A.1. The tests used the same nozzle and seed method as described in Section 2.3, and was run at approximately 5 m/s for each test. Flow speed was verified using a Dwyer inclined manometer, model 202/5. The nozzle was fitted with an Omega Engineering AHF-12240 electric air flow heater that was controlled by a Superior Electric Powerstat Variable transformer, model 3PN116C, to set the temperature at the nozzle exit. The nozzle was fitted with multiple copper meshes in order to improve the temperature uniformity at the exit.

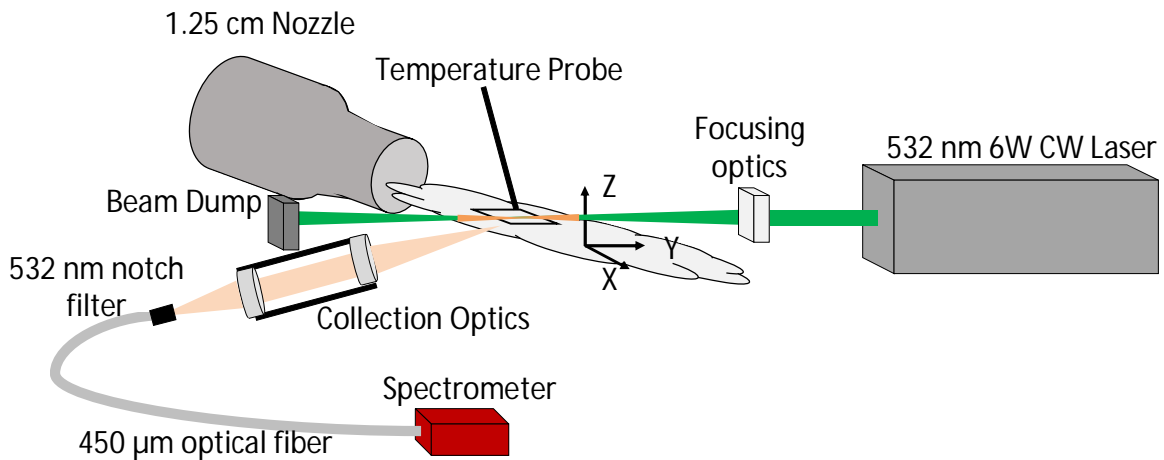


Figure A.1. Kiton Red thermometry test setup.

A Coherent Inc. Verdi V6 532 nm continuous wave laser operating at 6W provided the laser source for the Kiton Red particle LIF. The beam was focused to a point at the nozzle exit using a lens with focal length $f = 40$ mm. The fluorescence from particles in the path of the laser light is seen in Figure A.2. The fluorescent light was collimated and then focused using two lenses with focal lengths $f = 220$ mm and $f = 150$ mm, respectively. This light then passed through a 532 nm notch filter to block out all scattered light from the laser source. A 450 μm optical fiber collected this light and connected to a Thorlabs CCS175 spectrometer for LIF spectral measurements. The spectrometer recorded the fluorescence emissions spectrum over a set “integration time”, which

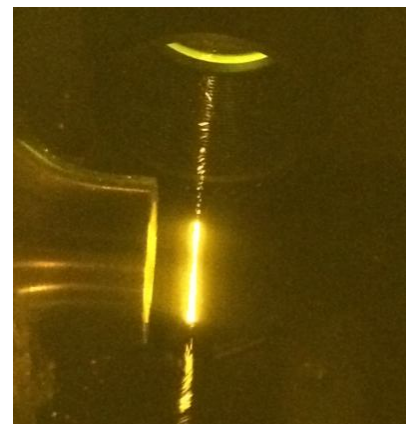


Figure A.2. Kiton Red particle fluorescent emission. Picture taken using optical filter to block all 532 nm laser light.

varied from test to test based on the seed output. It was desired to set an integration time where the fluorescence signal would occupy 50-75% of the dynamic range of the spectrometer. For all data included in the following sections, the time was between 1-2 seconds. The spectral accuracy of the spectrometer was reported by the manufacturers to be <0.6 nm FWHM at 633 nm.

The flow temperature was measured adjacent to the beam path using an Omega Engineering Type T thermocouple, model TT-t-30-36. More details of the temperature measurements and associated uncertainties can be found in Section A.4.

A.3 Selection of Wavelength Bands

The bounds of the wavelengths bands were set to maximize the sensitivity of the two-band ratio to temperature variations. First, a series of spectra were obtained for flows ranging from room temperature up to 110°C, which is slightly above the reported particle melting temperature of 100°C [8]. These spectra were corrected for wavelength sensitivity bias in the spectrometer and then normalized by their peak intensity, and are plotted in Figure A.3. The sharp cutoff at 548 nm and intensity spike around 655 nm were artifacts of the spectrometer and not reflective of the actual particle fluorescence spectrum.

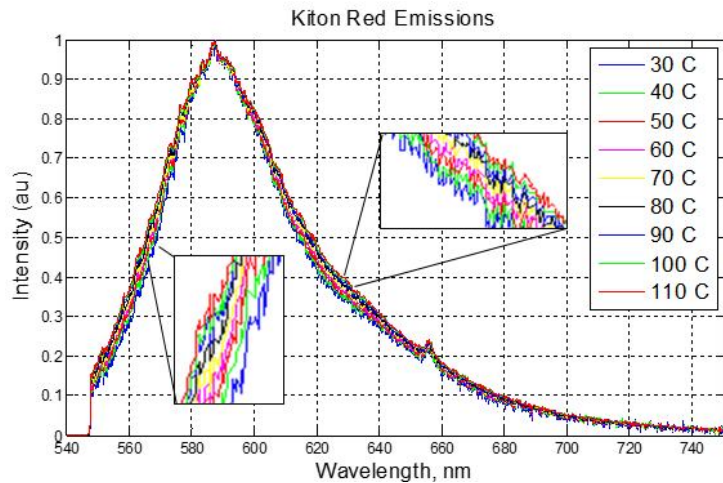


Figure A.3. Measured emission spectra of Kiton Red 620 doped PSLs at various temperatures.

The spectra in Figure A.3 do show a noticeable widening trend with increasing temperature. To determine which portions of the spectra are most sensitive to temperature, they were normalized by the spectrum at 70°C. Figure A.4 shows the results of this process for a few of the temperatures tested. There is a large region between 548 nm and about 580 nm where intensity increases with increasing temperature. Next is a region between about 580 and 600 nm where the spectra seem to decrease slightly with

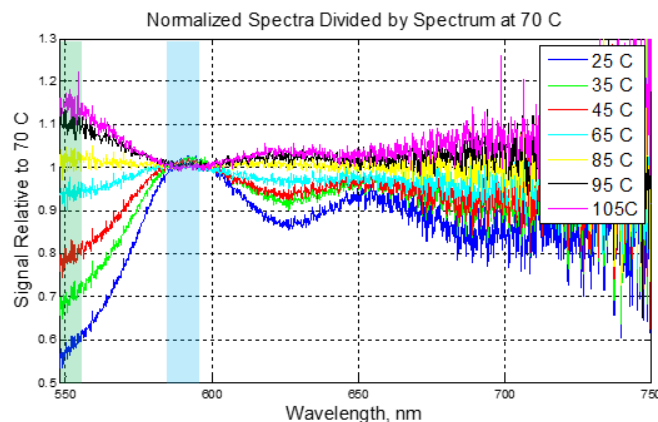


Figure A.4. Kiton Red 620 PSL emission spectra normalized by the spectrum at 70°C.

increasing temperature, followed by a region above 600 nm where intensity once again increases with increasing temperature.

An optimization code was written to sweep through all wavelengths between 548 and 750 nm to find two wavelength bands whose ratio had the largest relative change between room temperature and heated tests. Figure A.5 shows a few of the wavelength ranges tested. The wavelength bands whose ratio changed the most with changing temperature was found to be one band between 548 and 555 nm and another between 585 and 595 nm.

The bands are highlighted in Figure A.4. Intuitively, it makes sense that the largest fluctuations come from the ratio between a region with high temperature sensitivity and another region with slightly opposite sensitivity. For all future tests, the bands $548 < B_1 < 555$ nm and $585 < B_2 < 595$ nm were used for two-band ratio calculation.

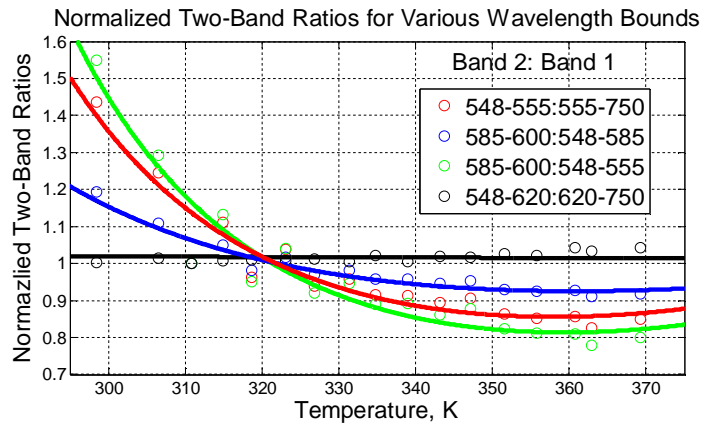


Figure A.5. Normalized two-band ratios for various wavelength bounds. Data sets were normalized by their measurements at 40°C.

A.4 Temperature Measurement Uncertainty

As stated in Section A.2, the temperature measurement for each calibration data point was taken at the center of the nozzle exit, adjacent to the beam path. The temperature was measured at 4 Hz over a period of approximately 10 seconds, and the fluorescent emissions spectrum of the seed particles was subsequently recorded. Then, the temperature was measured once again for another ten seconds. The average temperature value for these recordings was used as the particle temperature for the calibration curve.

There are three distinct sources of error in this measurement that contribute to the temperature uncertainty. First is the uncertainty in each individual temperature measurement, dT_a . This uncertainty is provided by the thermocouple manufacturer to be $\pm 0.5^\circ\text{C}$. Second is the uncertainty due to jet temperature unsteadiness. This uncertainty, dT_b , was quantified using twice the standard deviation of the temperature measurements for a given data set.

The final source of error is due to the assumption that the temperature measured at the center of the jet is uniform across the entire exit. While temperature was measured at only the single point, the light collected by the spectrometer comes from the fluorescent region across the whole jet exit. To quantify this, the temperature profile across the exit was measured and plotted in Figure A.6.

The figure shows a fairly uniform temperature distribution across the majority of the nozzle exit cross section. The assumption that the point measurement of temperature appropriately describes the temperature across the entire exit is estimated to be accurate within $dT_c = \pm 3^\circ\text{C}$. The overall uncertainty associated with a temperature was calculated using Equation A.4, which includes the results for the 30°C measurement as an example.

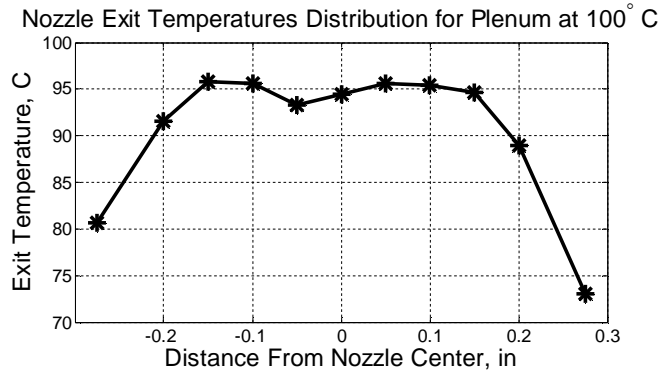


Figure A.6. Nozzle exit temperature distribution across exit cross section.

$$dT_{overall} = \sqrt{(dT_a)^2 + (dT_b)^2 + (dT_c)^2} = \sqrt{(0.5)^2 + (0.356)^2 + (3)^2} = \pm 3.1^\circ\text{C} \quad (\text{A.4})$$

A.5 Calibration Experimental Results

A calibration curve was generated for the Kiton Red 620 PSLs. For nozzle exit temperatures of approximately 30° , 50° , 70° , and 90°C , a total of ten spectra each were recorded. Five spectra at each temperature were obtained in ascending order, followed by the final five in descending order. For each spectrum, the two-band ratio using the bands defined in Section A.3 was calculated. The mean ratio at each temperature was calculated and plotted in Figure A.7.

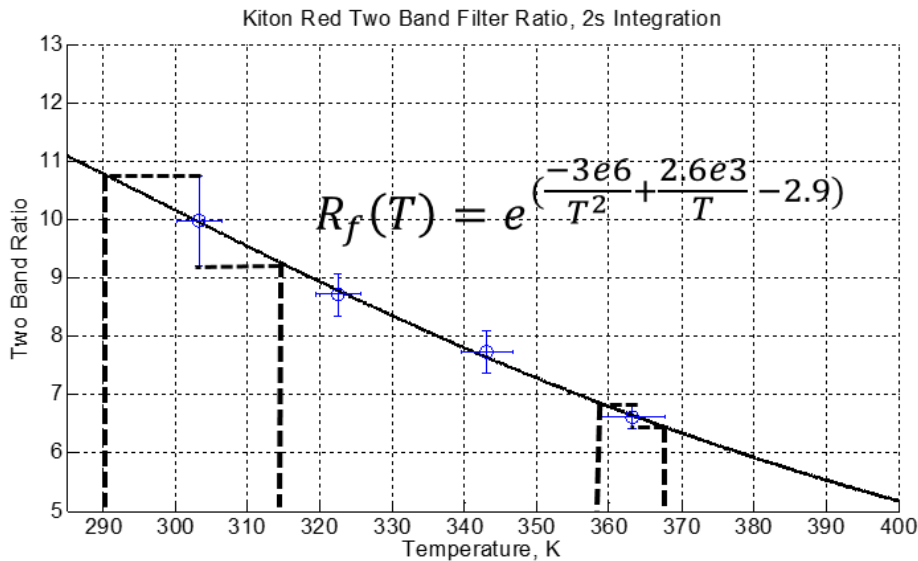


Figure A.7. Kiton Red particle two-band filter ratio calibration curve. Best fit equation also shown.

Uncertainty in the two-band ratio was calculated using a Student's t-distribution of the ten spectra at each temperature with 95% confidence intervals. Uncertainty in the measured temperature is calculated using Equation A.4. Finally, a curve of the form in Equation A.2 was fit to the data and is also plotted in Figure A.7.

While the data in Figure A.7 fits the expected curve closely, the uncertainties in each two-band ratio measurement are fairly high. They indicate a calibration uncertainty of approximately $\pm 12.5^\circ\text{C}$ at low temperatures and $\pm 4.5^\circ\text{C}$ at higher temperatures.

A.6 Conclusions

From the results presented above, it was concluded that the Kiton Red PSL particles did not exhibit enough temperature sensitivity relative to the measurement uncertainties to warrant further investigation. The calibration uncertainties achieved in this study were as high as $\pm 25^\circ\text{C}$, not including repeatability issues discovered during multi-day testing. Additional studies would be useful in determining the causes of this issue, which could be due to day-to-day variations in seeder output, flow heater patterns, or something else altogether. The investigation into the Kiton Red fluorescence variations due to temperature were discontinued to put more efforts into fluorescent PIV, which showed significantly more promise.

A.7 References

- [1] Lemoine F, Antoine Y, Wolff M and Lebouche M, "Simultaneous Temperature and 2D Velocity Measurements in a Turbulent Heated Jet Using Combined Laser-Induced Fluorescence and LDA," *Experiments in Fluids*, vol. 26, no. 4, pp. 315-323, 1999.
- [2] Hishida K and Sakakibara J, "Combined Planar Laser-Induced Fluorescence-Particle Image Velocimetry Technique for Velocity and Temperature Fields," *Experiments in Fluids*, vol. 29, no. 1, pp. S129-140, 2000.
- [3] Abram C, Fond B, Heyes A and Beyrau F, "High-Speed Planar Thermometry and Velocimetry Using Thermographic Phosphor Particles," *Applied Physics B*, vol. 111, no. 2, pp. 155-160, 2013.
- [4] Deprédurand V, Miron P, Labergue A, Wolff M and Castanet G, "A Temperature-Sensitive Tracer Suitable for Two-Colour Laser-Induced Fluorescence Thermometry Applied to Evaporating Fuel Droplets," *Measurement Science and Technology*, vol. 19, no. 10, 2008.
- [5] Lavieille P, Lemoine F, Lavergne G and Lebouché, "Evaporating and Combusting Droplet Temperature Measurements Using Two-Color Laser-Induced Fluorescence," *Experiments in Fluids*, vol. 31, no. 1, pp. 45-55, 2001.
- [6] Bruchhausen M, Guillard F and Lemoine F, "Instantaneous Measurement of Two-Dimensional Temperature Distributions by Means of Two-Color Planar Laser Induced Fluorescence (PLIF)," *Experiments in Fluids*, vol. 38, no. 1, pp. 123-131, 2005.
- [7] Lavieille P, Delconte A, Blondel D, Lebouché M and Lemoine F, "Non-Intrusive Temperature Measurements Using Three-Color Laser-Induced Fluorescence," *Experiments in Fluids*, vol. 36, no. 5, pp. 706-716, 2004.

- [8] Maisto P, "Experimental Analysis and Prospective Flow Diagnostic Applications for Fluorescence Dye-Doped Micro-Particles," M.S. Thesis, Aerospace and Ocean Engineering Department, Virginia Tech, Blacksburg, VA, 2014.